The Astrophysical Journal, 978:163 (19pp), 2025 January 10 https://doi.org/10.3847/1538-4357/ad9c76

SN 2014C: A Metamorphic Supernova Exploded in the Intricate and Hydrogen-rich Surroundings

Qian Zhai[1,2], Jujia Zhang[1,2,3], Weili Lin[4,5], Paolo Mazzali[6,7], Elena Pian[6,8], Stefano Benetti[9], Lina Tomasella[9], Jialian Liu[5], and Liping Li[1,2,3]

[1] Yunnan Observatories (YNAO), Chinese Academy of Sciences (CAS), Kunming, 650216, People's Republic of China; jujia@ynao.ac.cn
[2] Key Laboratory for the Structure and Evolution of Celestial Objects, CAS, Kunming, 650216, People's Republic of China
[3] International Centre of Supernovae, Yunnan Key Laboratory, Kunming 650216, People's Republic of China
[4] Department of Astronomy, Xiamen University, Xiamen, Fujian 361005, People's Republic of China
[5] Physics Department and Tsinghua Center for Astrophysics (THCA), Tsinghua University, Beijing 100084, People's Republic of China
[6] Astrophysics Research Institute, Liverpool John Moores University, Liverpool Science Park, 146 Brownlow Hill, Liverpool L3 5RF, UK
[7] Max-Planck-Institut für Astrophysik, Karl-Schwarzschild Straße 1, 85748 Garching, Germany
[8] INAF, Astrophysics and Space Science Observatory, Via P. Gobetti 101, 40129 Bologna, Italy
[9] INAF—Osservatorio Astronomico di Padova, Vicolo dell'Osservatorio 5, I-35122 Padova, Italy
Received 2024 July 11; revised 2024 December 04; accepted 2024 December 06; published 2025 January 10

Abstract

We present photometric and spectroscopic observations of supernova (SN) SN 2014C, primarily emphasizing the initial month after the explosion at approximately daily intervals. During this time, it was classified as a Type Ib SN exhibiting a notably higher peak luminosity ($L_{\rm peak} \approx 4.3 \times 10^{42}\,{\rm erg\,s^{-1}}$), a faster rise to brightness ($t_{\rm rise} \approx 11.6$ days), and a more gradual dimming ($\Delta m_{15}^{V} \approx 0.48$ mag) compared to typical Type Ib SNe. Analysis of the velocity evolution over the first ~20 days after the explosion supports the view that the absorption near 6200 Å is due to high-velocity Hα in the outer layers of the ejecta, indicating the presence of a small amount of hydrogen in the envelope of the progenitor before the explosion. Assuming that the peak luminosity is entirely attributed to radioactive decay, we estimate that 0.14 $M_{\odot}$ of ^{56}Ni was synthesized in the explosion. However, this amount of nickel could no longer maintain observed brightness approximately 10 days after peak luminosity, suggesting additional energy sources beyond radioactive decay. This supplementary energy likely originates from interaction with the circumstellar medium (CSM). Consequently, the timing of the SN−CSM interaction in SN 2014C may occur much earlier than the emergence of Type IIn−like features during the nebular phase.

Unified Astronomy Thesaurus concepts: Type Ib supernovae (1729); Supernovae (1668); Core-collapse supernovae (304)

Materials only available in the online version of record: data behind figures

1. Introduction

Stripped-envelope supernovae (SESNe) are the explosion of a massive star that has lost its hydrogen or helium envelopes either through stellar winds (J. H. Groh et al. 2014) or via mass transfer to a companion star (S. C. Yoon et al. 2010). However, the processes by which a massive progenitor undergoes envelope stripping during the core collapse and the state of the circumstellar material (CSM) at the time of the certain SESN explosion remain highly complex and not fully understood.

Recent observations of stellar explosions show that massive stars often experience complex mass loss before death. These include pre-explosion eruptions in H-rich stars, progenitors of ordinary Type IIn SNe (SNe IIn; M. Fraser et al. 2013; J. C. Mauerhan et al. 2013a, 2013b; A. Pastorello et al. 2013; J. L. Prieto et al. 2013; J. Mauerhan et al. 2014; E. O. Ofek et al. 2014; N. Smith 2014), and progenitors of SNe IIp that experience short-lived interactions with CSM (L. Dessart et al. 2017; O. Yaron et al. 2017; W. V. Jacobson-Galán et al. 2024; J. Zhang et al. 2023, 2024). Even H-poor progenitors show erratic mass-loss behavior preceding core collapse (A. Pastorello et al. 2007; S. Immler et al. 2008; R. J. Foley et al. 2011; A. Gal-Yam et al. 2014; K. Maeda et al. 2015). This time-dependent mass loss differs from the steady loss assumed in current models. The cause of this highly variable mass loss is debated, and its role in the evolution of the progenitor remains unclear.

SN 2014C showed a remarkable metamorphosis from a hydrogen-poor (H-poor) SN Ib to an SN interacting with hydrogen-rich (H-rich) CSM, characterized by the intermediate broadening of an Hα emission line at about 100 days after the explosion (D. Milisavljevic et al. 2015; R. Margutti et al. 2017). This shift arises from the interaction between SN and CSM, presenting a rare chance to study the mass loss of its progenitor leading up to the explosion. Some investigations on the later phase of SN 2014C have been published, particularly regarding the properties of sounding CSM derived by the interaction signal (S. Tinyanont et al. 2016, 2019; G. E. Anderson et al. 2017; M. F. Bietenholz et al. 2018, 2021; D. Brethauer et al. 2022; B. P. Thomas et al. 2022). These observations suggest that SN 2014C exploded inside a low-density cavity and the expanding shock encountered a dense H-rich shell within a year after the explosion.

The transition from SNe Ib/c to SNe IIn, attributed to interactions with H-rich CSM, has been documented in multiple cases, including SN 2001em (N. N. Chugai & R. A. Chevalier 2006; P. Chandra et al. 2020), SN 2004dk (J. C. Mauerhan et al. 2018), SN 2019oys (J. Sollerman et al. 2020), and SN 2019yvr

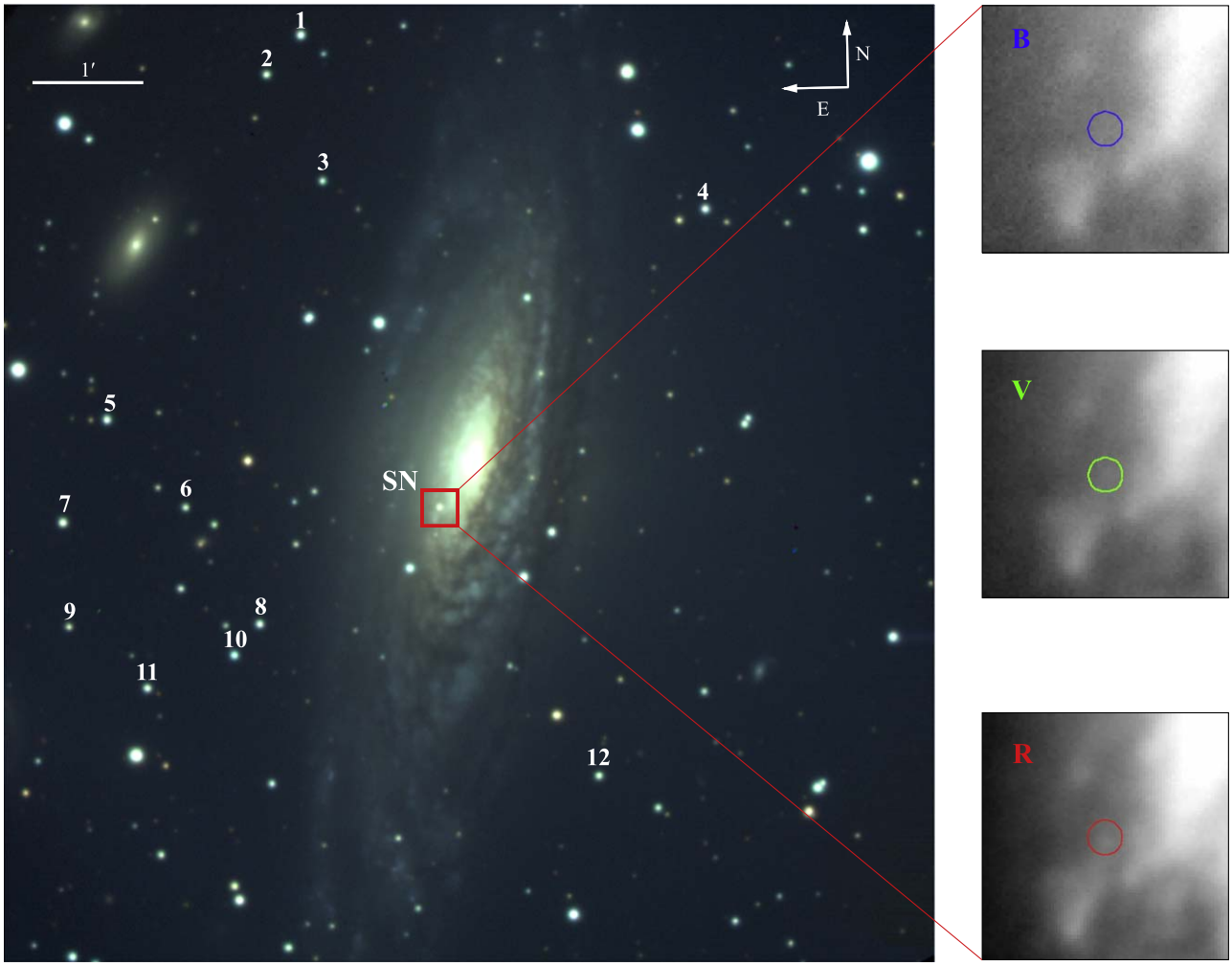

Figure 1. Finder chart of SN 2014C and its local reference stars, combined by *BVR*-band images taken by the LJT and YFOSC in 2014 January. The mean FWHM of the combined image is ~1.″50 under the scale of ~0.″28 pixel^{-1}. The zoomed-in templates taken in 2020 November for the *BVR* bands, which encompass the region containing SN 2014C, are presented on the right.

(N.-C. Sun et al. 2022; L. Ferrari et al. 2024), among others. These SNe exhibit varying timing and intensity of interactions, indicative of differences in the geometry and density of CSM.

However, the relationship between these changes and SN explosion parameters needs to be confirmed. This uncertainty primarily arises from our limited understanding of the explosion properties of these peculiar SNe. They usually attract attention later when significant interaction signals are detected, with insufficient early observations. For instance, SN 2001em and SN 2019oys have only one low-quality identification spectrum from their early phases.

SN 2014C posed a similar challenge. Shortly after the explosion, its position behind the Sun restricted observations, limiting researcher interest. Notably, only two early spectra have been published (D. Milisavljevic et al. 2015; B. P. Thomas et al. 2022), which is insufficient for determining the evolutionary trend during the SN Ib phase. Furthermore, early photometric results (R. Margutti et al. 2017) may have overestimated the luminosity of this SN, particularly during its rise and decline, due to the absence of host galaxy template subtraction.

Here we present spectra from the first month after the explosion, including nearly daily observations in the initial 2 weeks. Through template subtraction using pre- and post-explosion images, we have improved the photometry of this SN. Analysis of these observations enables us to investigate many explosion properties, which are crucial for understanding the mechanisms of this extraordinary event.

The manuscript is organized as follows: Observations and data reductions are described in Section 2. Section 3 presents the UV and optical light and color curves, while Section 4 presents the spectral evolution. In Section 5, we calculate and analyze the bolometric light curve of SN 2014C. Finally, a summary is provided in Section 6.

2. Observations and Data Reduction

SN 2014C was discovered in an unfiltered image of the spiral galaxy NGC 7331 (W. Zheng et al. 2014) taken on 2014 January 5.09 UT (UT is used throughout this paper) using the 0.76 m Katzman Automatic Imaging Telescope (KAIT) at Lick Observatory. It was also detected 3 days earlier on a pre-discovery image taken on January 2.10 UT by KAIT (W. Zheng et al. 2014). The coordinates of this SN are R.A. = $22^{h}37^{m}5\overset{s}{.}6$, decl. = $+34°24'31\overset{''}{.}9$ (J2000), located at $19\overset{''}{.}7$ east and $24\overset{''}{.}2$ south of the center of the host galaxy, as shown in Figure 1. Given the Cepheids distance of NGC 7331, $D = 15.1 \pm 0.7$ Mpc (B. Kumar et al. 2013), the distance from SN 2014C to the host center is about 2.2 kpc.

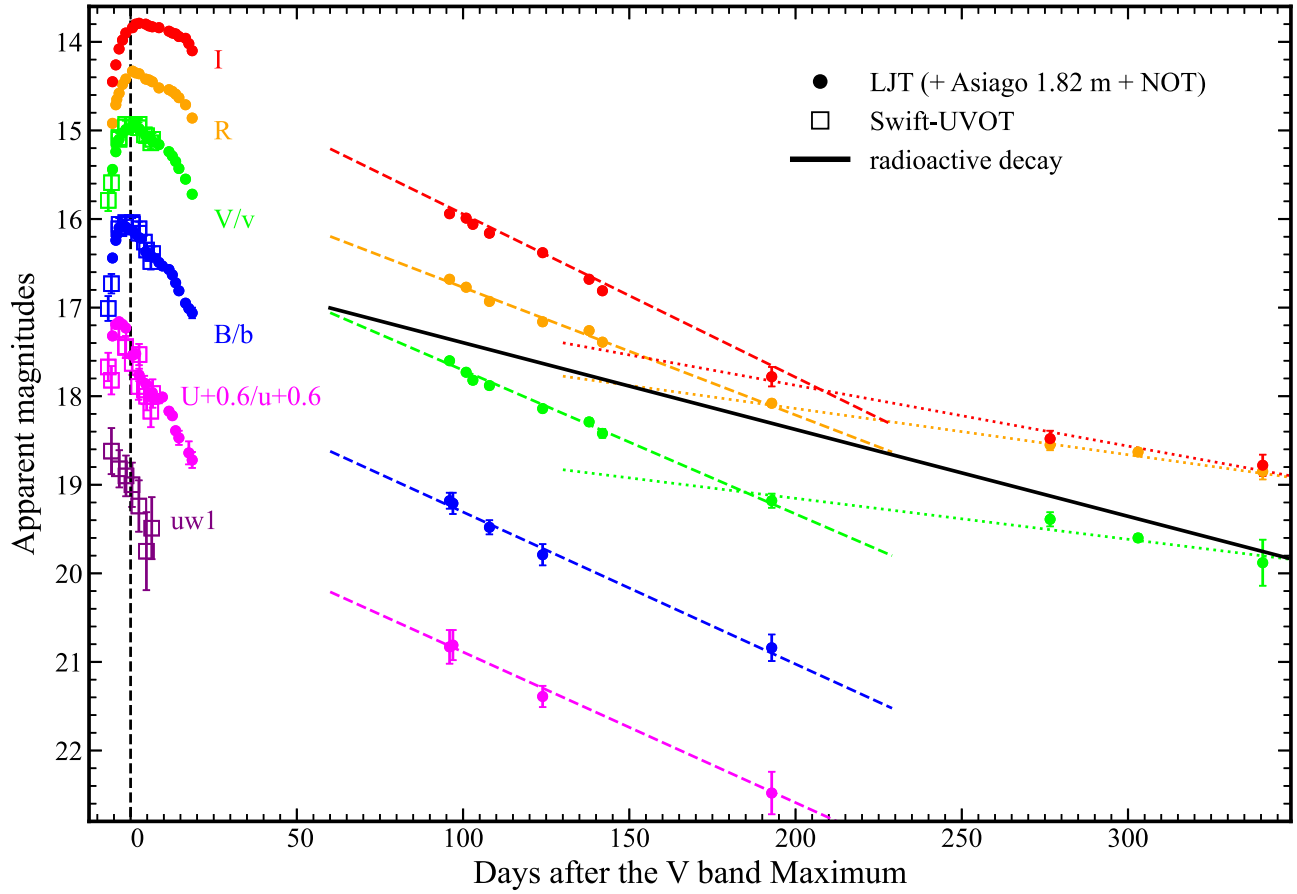

Figure 2. *UBVRI*-band and *uw*1-, *u*-, *b*-, and *v*-band light curves of SN 2014C. The dashed and dotted lines are the linear fit of the *UBVRI*-band light curve at the tail phase. The solid line is the RD rate (i.e., 0.98 mag/100 days) from ^{56}Co to ^{56}Fe.

This transient was identified as a young SN Ib (M. Kim et al. 2014) on January 5.54 by the Lijiang 2.4 m telescope (LJT) at Lijiang Observatory of Yunnan Astronomical Observatory (YNAO; Y.-F. Fan et al. 2015) with the Yunnan Faint Object Spectrograph and Camera (YFOSC; C.-J. Wang et al. 2019). Cross-correlation with a library of SN spectra using the "supernova identification" code (SNID; S. Blondin & J. L. Tonry 2007) shows that SN 2014C matches with SN Ib 1999ex at $t \approx -6$ days after brightness maximum (hereafter variable t denotes the time since V-band maximum and τ denotes the time since the explosion).

We triggered the LJT follow-up observing campaign for this young SN, especially at a daily cadence in the first month after discovery. The monitoring spans from $t \approx -7$ days to $t \approx +340$ days. High-quality template images taken by the LJT+YFOSC at ~2500 days after the explosion are applied to the image subtraction for better photometry. Besides, the UV−optical photometry spanning from $t \approx -7$ days to $t \approx +7$ days of Swift-UVOT (N. Gehrels et al. 2004; P. W. A. Roming et al. 2005) is involved in this paper.

2.1. Photometry

The photometry of SN 2014C is presented in Figure 2, covering about the first year after the explosion, including the photometry of the LJT with YFOSC, the Asiago 1.82 m Copernico telescope with the Asiago Faint Object Spectrograph and Camera (AFOSC), and the 2.56 m Nordic Optical Telescope (NOT) with the Alhambra Faint Object Spectrograph and Camera (ALFOSC). The Johnson–Bessell *UBVRI*-band image of SN 2014C was reduced using the standard procedures of Pyraf (Science Software Branch at STScI 2012), including corrections for bias, overscan, flat-fielding, and cosmic-ray removal. Twelve local reference stars in the field of this SN are marked in Figure 1. The instrumental magnitudes of these reference stars are converted to the standard *UBVRI* system in the Vega magnitude by a transformation established by observing a series of Landolt standard stars on some photometric nights. These magnitudes were applied to calibrate the photometry of SN 2014C, as presented in Table A2.

The photometry of SN 2014C obtained with Swift-UVOT in one UV filter (*uvw*1) and three broadband optical filters (*u*, *b*, and *v*) is presented in Table A3. The photometry presented here was reduced using the Swift Optical/Ultraviolet Supernova Archive (SOUSA; P. J. Brown et al. 2014) reduction, which includes subtraction of the host galaxy flux using Swift-UVOT observations from 2007 May and 2013 April. Table A3 lists the final UVOT UV/optical magnitudes of SN 2014C. The optical magnitudes derived by SOUSA match the *UBV*-band magnitudes obtained by the LJT on scales smaller than 0.05 mag. However, the Swift-UVOT photometry in R. Margutti et al. (2017) is ~0.2–0.6 mag brighter than that of SOUSA in the *u*, *b*, and *v* bands and is ~1.0 mag in the *uvw*1 band.

The discrepancy between the two data sets exhibits an inverse proportionality to both the observation wavelength and the brightness of the SN, which is commonly associated with measurement errors due to host background contamination.

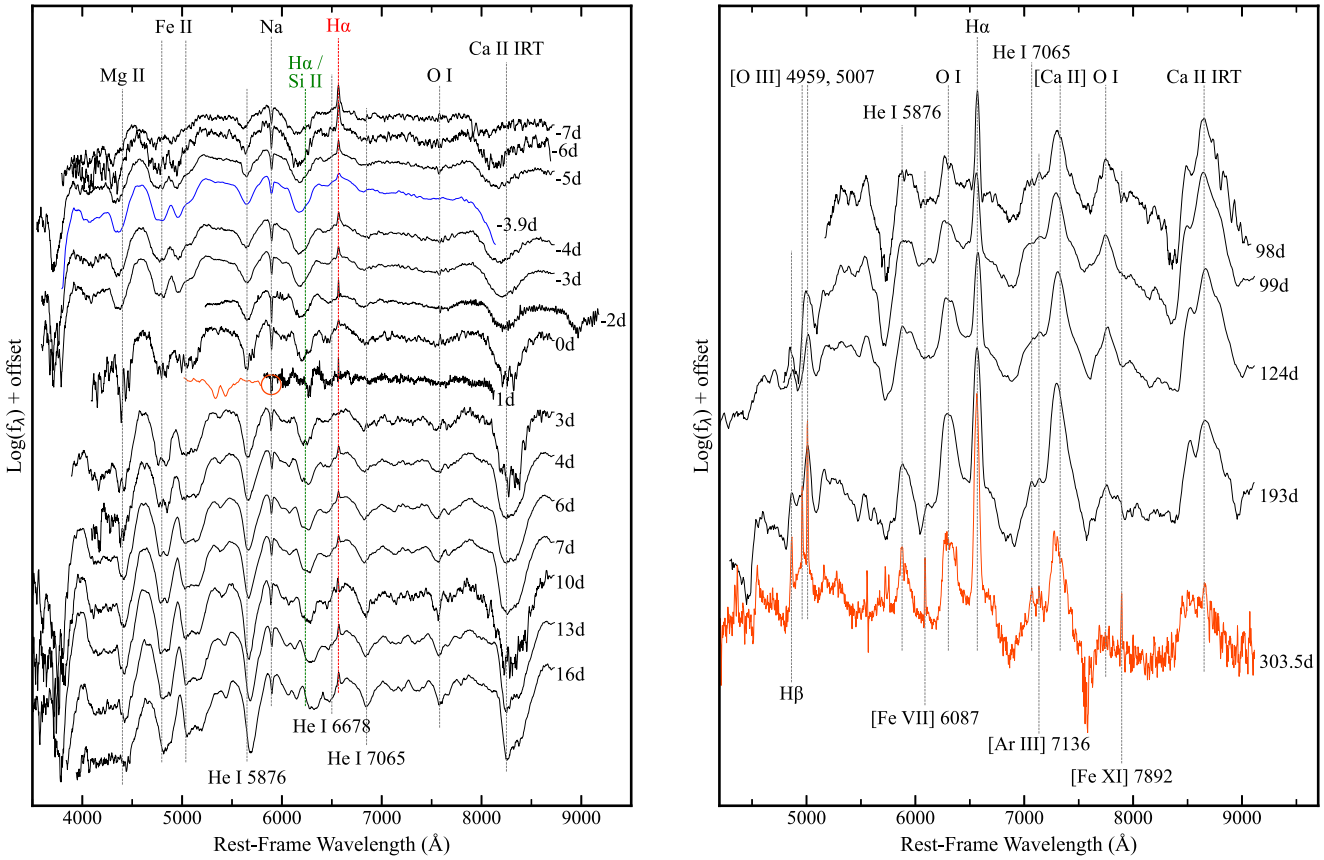

Figure 3. Spectra of SN 2014C obtained by the LJT (black), the Asiago 1.82 m telescope (blue), and NOT (orange-red). These spectra are shifted vertically for clarity and labeled according to the phase referring to the *V*-band maximum. A bin size = 6 pixels was applied to improve the signal-to-noise ratio of each spectrum. The region around the center wavelength of Na I D lines at $t \approx 1$ day is zoomed in. The red dotted line marks the Hα emission from background contamination. (The data used to create this figure are available in the online article.)

The measurements reported in R. Margutti et al. (2017) did not incorporate template subtraction, resulting in an overestimated brightness. Around peak brightness, the difference in the optical bands narrows to approximately 0.2 mag. Therefore, while significant discrepancies exist during the early stages, the two measurements of peak luminosity are generally consistent.

2.2. Spectroscopy

Figure 3 shows spectra of SN 2014C obtained by the LJT (+YFOSC), the Asiago 1.82 m telescope (+AFOSC; classification spectrum presented in M. Kim et al. 2014), and NOT (+ALFOSC) covering about 300 days since 2014 January 5. Observational journals for these spectra are listed in Table A4. All of these spectra were calibrated in both wavelength and flux and were corrected for telluric absorption and redshift. The flux of the continuum was then cross-checked with the synthetic photometry computed using the Johnson–Bessell passbands.

2.3. Reddening

The early spectra of SN 2014C exhibit significant absorption of narrow Na I D from the host galaxy. For instance, the mid-resolution spectrum at $t \sim +1$ day reveals resolved doublets of sodium, indicating substantial line-of-sight reddening toward the SN.

Despite the notable scatter in the data (e.g., D. Poznanski et al. 2011; M. M. Phillips et al. 2013), the equivalent width (EW) of Na I D absorption serves as a tool to roughly estimate the reddening based on empirical correlations. For example, correlations such as $E(B-V) = 0.16\,\mathrm{EW_{Na}} - 0.01$ (M. Turatto et al. 2003) and $E(B-V) = 0.25\,\mathrm{EW_{Na}}$ (R. Barbon et al. 1990) can be applied. The measured EW (Na I D) of SN 2014C was 3.19 ± 0.08 Å, corresponding to an average color excess of $E(B-V)_{\rm host} = 0.65 \pm 0.20$ mag following these relations. This value aligns closely with the estimation provided by D. Milisavljevic et al. (2015), which yields $E(B-V)_{\rm host} = 0.67$ mag using the same methodology.

Based on a broader sample of SNe Ib/c, M. R. Drout et al. (2011) proposed estimating host galaxy reddening photometrically. They found that the $V-R$ color of extinction-corrected SNe Ib/c clusters tightly around 0.26 ± 0.06 mag at $t \approx +10$ days after the *V*-band maximum and 0.29 ± 0.08 mag at $t \approx +10$ days after the *R*-band maximum. This method yields an estimate of $E(B-V)_{\rm total} = 0.67 \pm 0.05$ mag for SN 2014C, assuming an $R_V = 3.1$ Milky Way extinction law for the host galaxy. Considering the Galactic extinction $E(B-V)_{\rm Gal} = 0.08 \pm 0.01$ (E. F. Schlafly & D. P. Finkbeiner 2011), the host reddening derived from the $V-R$ color is $E(B-V)_{\rm host} = 0.59 \pm 0.05$ mag.

Considering the results of Na I D absorption and $V-R$ color, the average value of host galaxy reddening is $E(B-V)_{\rm Host} = 0.62 \pm 0.10$ mag, and the total extinction adopted for subsequent calculations is $E(B-V) = 0.7 \pm 0.1$ mag.

3. Photometric Analysis

3.1. Light Curves

Figure 2 shows the photometric evolution of SN 2014C in the first year after the explosion. The light-curve parameters of SN 2014C, estimated by low-order polynomial fitting, are presented in Table 1. These include the peak time (t_{max}), rise time (t_{rise}), peak magnitude (m_{peak}), absolute magnitude (M_{peak}), and post-maximum decline of the light curve in 15 days (Δm_{15}), which are listed in Table 1.

Based on the pre-discovery detection in the clear band from KAIT images and LJT follow-up in the *R* band, we derived the explosion date of SN 2014C to be MJD = 56658.91 via fireball fitting, as seen in Figure 4. The fireball model assumes that the photosphere expands uniformly while its surface luminosity remains constant (W. D. Arnett 1982). Our estimated explosion date aligns well with the phase via SNID fitting of our identification spectrum. However, the explosion time inferred using the fireball model may have limitations for SNe Ib/c. For instance, some SNe Ib/c, such as SN 2005bf and SN 2008D (Figure 4), exhibit two peaks in their early light curves, potentially attributed to shock breakout and subsequent cooling effects. Due to the absence of sufficiently close and deep nondetection data before the first detection of SN 2014C, its actual explosion time may precede the fireball model estimates. With available data and assumptions about typical supernova evolution, R. Margutti et al. (2017) estimated MJD = 56656 as the explosion date. A. L. Piro & E. Nakar (2013) discuss additional uncertainty in estimating the time of explosion from a simple extrapolation of the light curve.

Besides SN 2005bf and SN 2008D, Figure 4 also displays the *UBVRI*-band light-curve comparisons with other well-sampled SNe Ib/c, including two SN 2014C−like metamorphic SNe, SN 2019oys and SN 2019yvr, which both displayed SN−CSM interaction signatures in their nebular spectra. The *r*- and *i*-band light curves of SN 2005bf, SN 2007Y, and SN 2019yvr and the i'-band light curve of SN 2005hg are plotted in this figure owing to the lack of observations in Johnson *RI* bands. Table A5 lists the *R*/*r*-band parameters of these samples.

SN 2014C reaches its *R*-band peak approximately 12 days after the explosion, which is faster than the rise times of the other SNe Ib/c. To minimize the influence of the shock cooling phase (as observed in SN 2008D and SN 2005bf) and focus on the luminosity increase driven by radioactive decay (RD) and photospheric expansion, we computed the duration for the luminosity to ascend from half of its peak value to the peak. Even among all the samples listed in Table A5, SN 2014C exhibited the swiftest rise, attaining peak luminosity from half its maximum brightness in $t_{1/2}^{R} \approx 7.3$ days, half the typical rise time for SNe Ib.

The rise time of SN depends on factors such as the ejecta mass and explosion energy, with a fast rise potentially indicating a high ratio of explosion energy to ejecta mass (e.g., K. Nomoto et al. 1994). Additionally, the width of the light curve is sensitive to the photon diffusion time relative to the explosion kinetic energy and ejecta mass. A small progenitor radius at the time of explosion can lead to a rapid rise due to a short dynamical timescale. Moreover, a small amount of ^{56}Ni synthesized in the explosion can also result in a fast rise if the light curve is primarily powered by RD, as observed in SNe Ia (W. D. Arnett 1982).

However, SN 2014C exhibits a relatively higher peak luminosity, e.g., $M_{max}^{V} \approx -18.1$ mag, compared to the average value of SNe Ib, e.g., $M_{max}^{V} \approx -17$ mag (F. Taddia et al. 2018). As depicted in Figure 4, among the comparison samples, only the peculiar SN Ib/c SN 2005bf shows a brighter peak than SN 2014C in the *U* and *B* bands, while they are similar in the *VRI* bands. Additionally, SN 2011fu and SN 2009jf display similar peak brightness to SN 2014C, but they exhibit a brighter nebular phase than SN 2014C.

Table 1
UBVRI-band Parameters of SN 2014C

Band	t_{max} (MJD)	t_{rise} (days)	m_{peak} (mag)	M_{peak} (mag)	Δm_{15} (mag)
U	56666.48	7.57	16.54	−17.76	1.00
B	56668.62	9.71	16.05	−17.70	0.62
V	56669.97	11.47	14.95	−18.11	0.48
R	56671.04	12.13	14.34	−18.22	0.33
I	56672.87	13.96	13.79	−18.21	0.26

Among these SNe, the decline of SN 2005bf is faster owing to the progenitor losing almost all of its envelope before exploding, with no observed interaction between the ejecta and the preceding slow stellar wind. The slow decline rate of the light curve in SN 2014C, SN 2009jf, and SN 2011fu suggests some form of interaction or additional energy sources. Nevertheless, SN 2014C declines more slowly than the comparison samples. A plateau-like structure can be observed in the *BVRI* band from 10 to 20 days after the peak brightness. Suppose that this plateau is caused by the kinetic energy of the ejecta being transferred owing to the SN −CSM interaction. In that case, a hydrogen envelope shell might exist at a distance from SN of 2×10^{15} cm to 3×10^{15} cm, assuming an expanding velocity of 10,000 km s^{-1}.

Between 100 days $< t <$ 200 days, the decline rate of SN 2014C is faster than expectations from RD of ^{56}Co, suggesting the presence of γ-ray leakage during this period. Conversely, at $t \gtrsim 200$ days, the light-curve decline rate decelerates relative to the RD rate, implying additional energy sources beyond the decay of ^{56}Co. As shown in Figure 4, despite significant SN −CSM interaction signals observed in its nebular spectra, the luminosity of SN 2014C at $t <$ 200 days did not decline significantly more slowly than that of other SNe Ib relative to their peak brightness. During a similar time frame, SN 2019oys and SN 2019yvr exhibited a more gradual decline in their light curves, with SN 2019oys even experiencing rebrightening at $t >$ 140 days. The diversity among these metamorphic SNe suggests variations in the efficiency of converting shock kinetic energy into radiation through the SN−CSM interaction.

3.2. Color Curves

Figure 5 illustrates the color curves of SN 2014C alongside some comparison samples. All color curves have been corrected for reddening using the $E(B-V)$ values listed in Table A5, assuming an extinction law with $R_V = 3.1$. In this figure, SN 2014C exhibits a relatively red color in $U-B$ and $B-V$, while displaying a blue color in $V-R$ and $V-I$, suggesting differences in energy distribution and temperature evolution.

In the early phase, contrary to the "U-turn" profile observed in most comparison samples, all color curves of SN 2014C show a monotonically decreasing trend from blue to red, indicating a decrease in temperature for this SN at $t \lesssim 5$ days. Between $t \sim 5$ and 20 days, the $U-B$ and $B-V$ color curves of SN 2014C

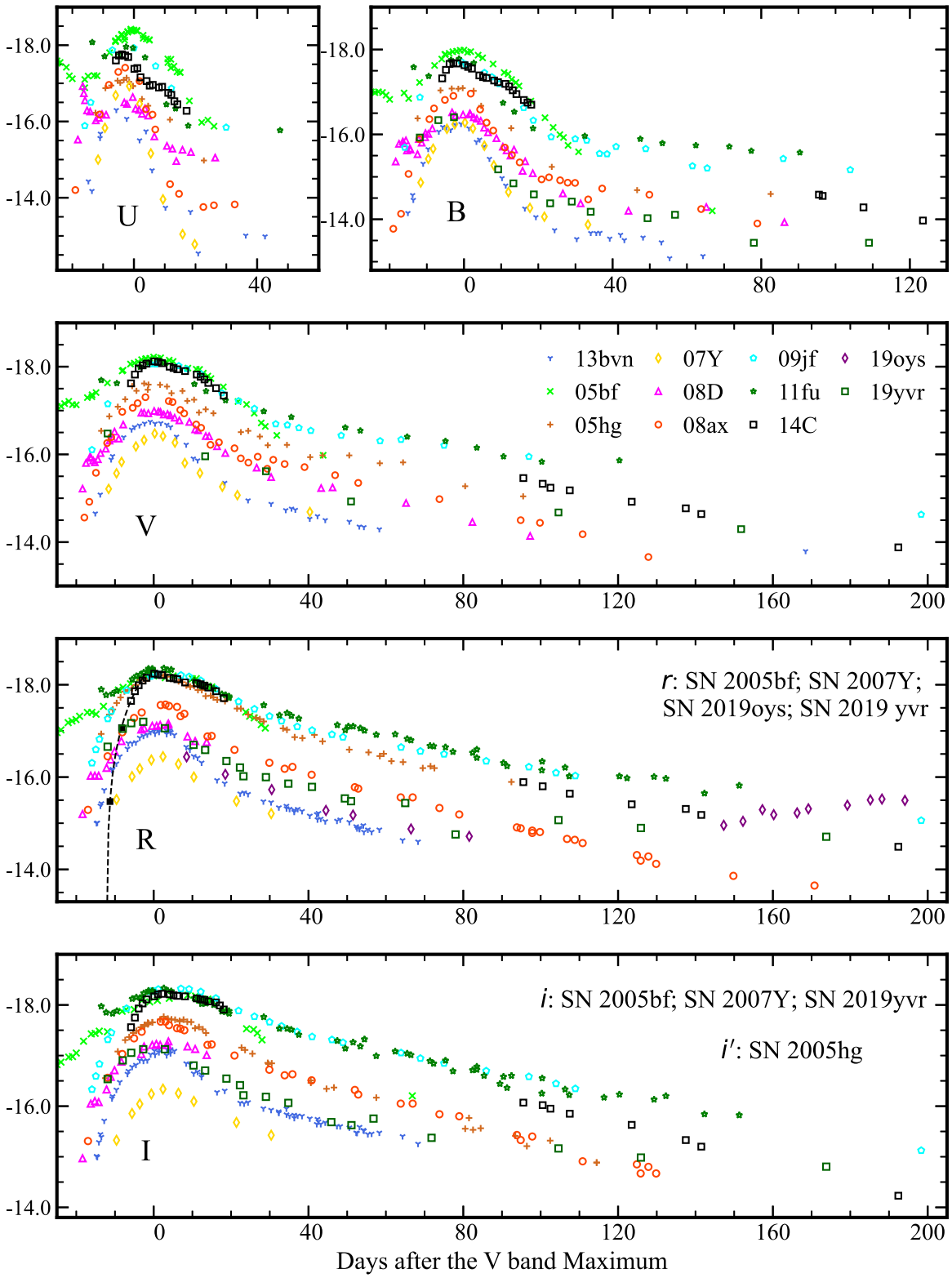

Figure 4. *UBVRI*-band absolute light curves of SN 2014C, compared with the light curves of some well-studied SESNe. The two filled squares mark photometry from unfiltered KAIT images obtained on January 5.09 (MJD 56659.10) and from earlier red magnitudes on a pre-discovery image taken on January 2.10 (MJD 56662.09; W. Zheng et al. 2014). A power-law fit (dashed line) is used with this photometry (filled squares) and the first three *R*-band measurements. The absolute magnitudes have been temporally shifted to the epoch of maximum brightness in the *V* band.

stabilize, while its $V-R$ and $V-I$ colors appear bluer compared to the comparison sample. This observation may be linked to the plateau-like structure observed in the light curves during this phase. Furthermore, at later times ($t \gtrsim 120$ days), the nebular $V-I$ color of SN 2014C becomes even bluer compared to its earlier state. This change can be attributed to an increased flux of Hα emissions resulting from interactions between SN and CSM, as evident from nebular spectra.

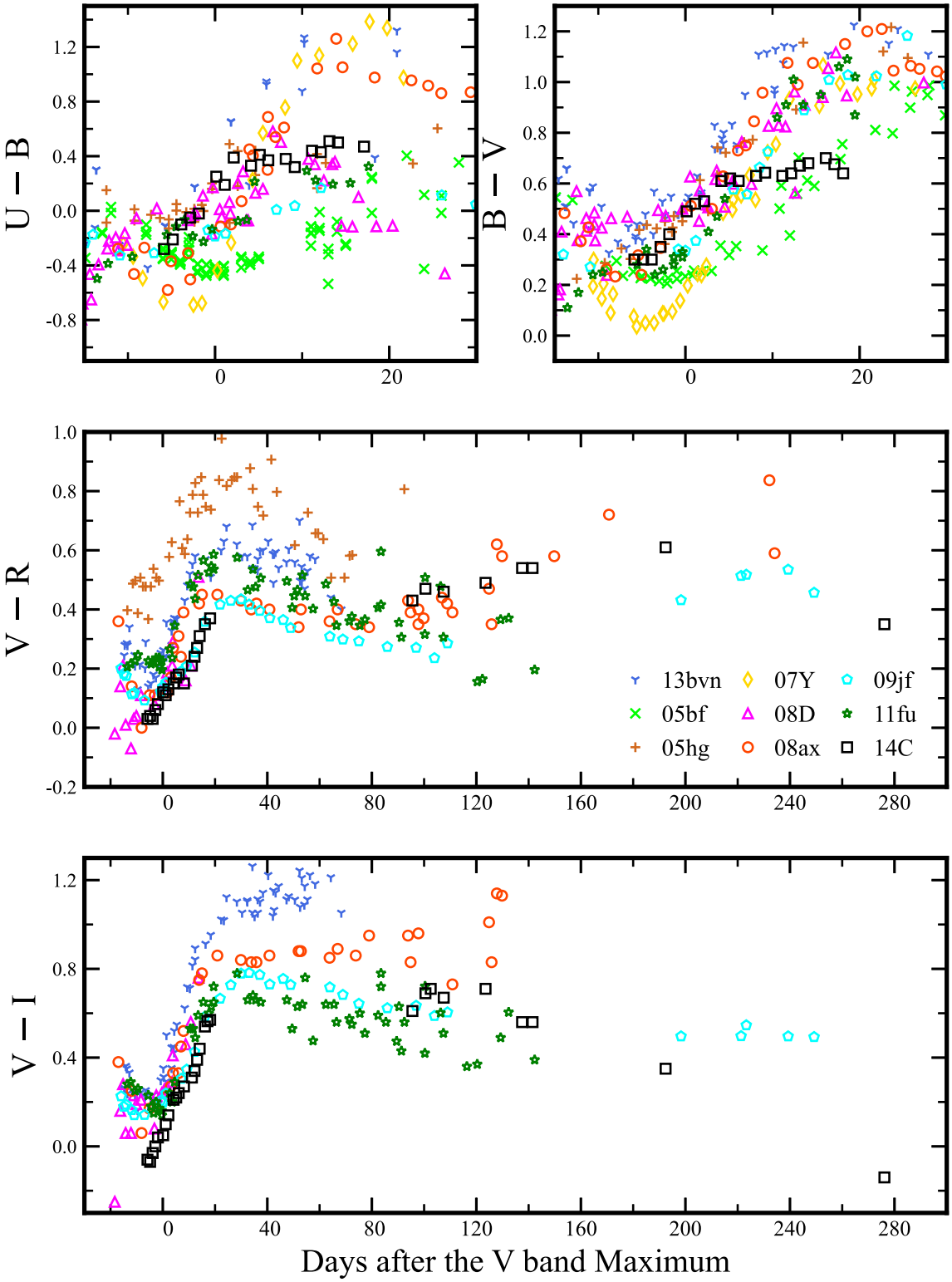

Figure 5. Color curves of SN 2014C comparing with other SNe Ib/c. All of these samples were corrected with reddening.

4. Spectra Analysis

4.1. First Month

In the left panel of Figure 3, densely sampled spectra reveal clear blueshifted He I $\lambda\lambda$5876, 7065 lines in the first month after the explosion, classifying SN 2014C as an SN Ib (P. A. Mazzali et al. 2008; A. M. Soderberg et al. 2008). Besides, these spectra are dominated by the following features: (1) absorption between 4400 and 4600 Å attributed to Mg II, (2) two absorption lines at ~5000 Å caused by Fe II, (3) a gradually strengthening O I λ7774 absorption, and (4) the blended Ca II $\lambda\lambda$8498, 8542, 8662 triplets at the red end.

An absorption feature around 6200 Å may arise from Hα or Si II λ6355. D. Milisavljevic et al. (2015) proposed that this

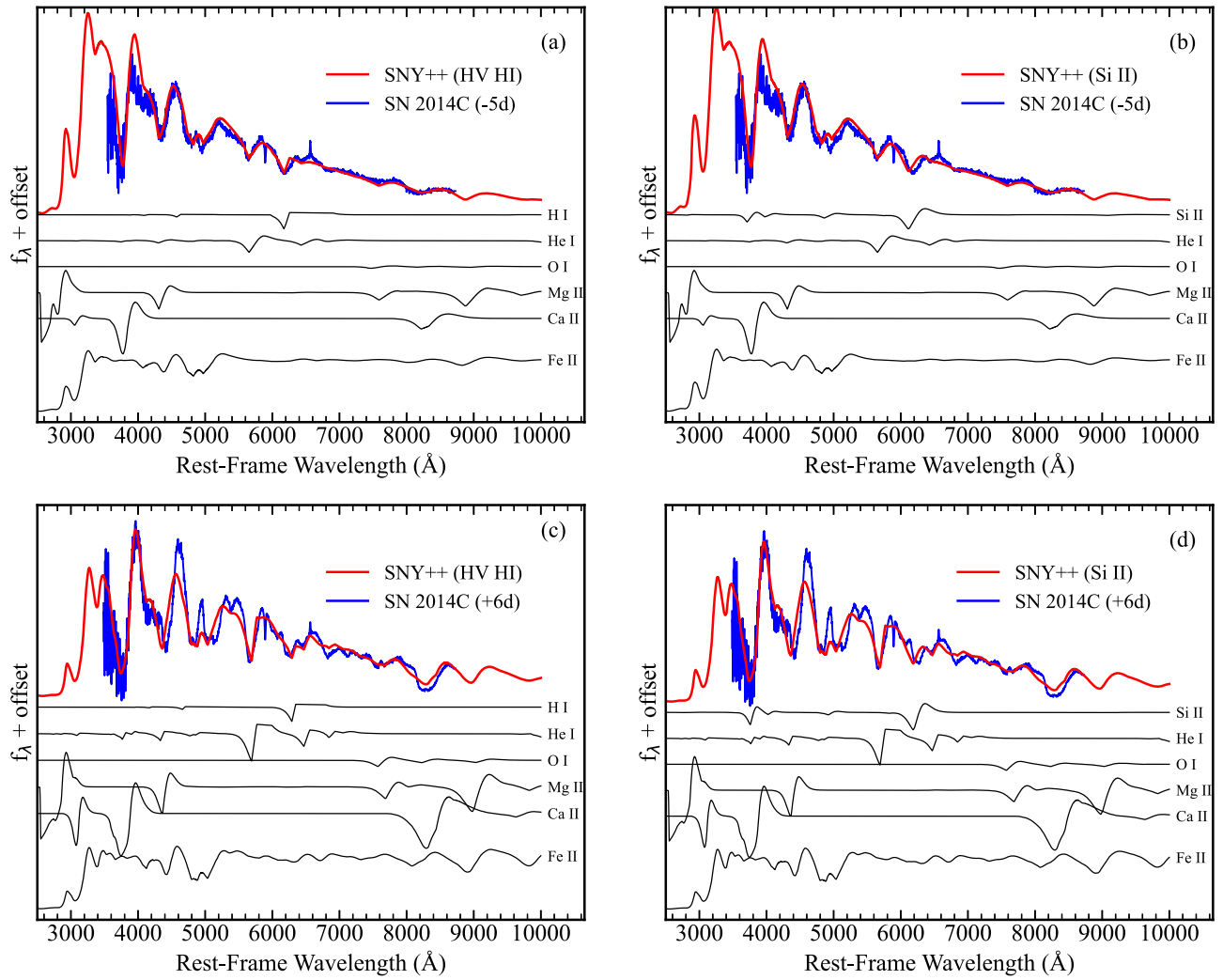

Figure 6. Spectra of SN 2014C at −5 days and +6 days reproduced by SYN++, including the element of H (panels (a) and (c)) and Si (panels (b) and (d)), respectively.

feature stems from high-velocity Hα and successfully reproduced the spectrum at $t \approx -4$ days within the elementary supernova spectrum synthesis code (SYN++; R. C. Thomas et al. 2011). Nonetheless, it is crucial to acknowledge that their analysis was limited to a single early spectrum, precluding further inferences based on the evolution of this absorption feature. However, as illustrated in Figure 6, both high-velocity Hα and the photospheric Si II λ6355 can fit the pre-maximum spectra within SYN++. The origin of this absorption is better constrained by examining multiple early spectra and tracing its evolutionary path.

Figure 7 illustrates the velocity evolution of this absorption component under the assumptions of Hα or Si II λ6355, comparing it to the velocities of He I and Ca II. These velocities decrease over time owing to the decreasing material velocity as the SN ejecta undergoes homologous expansion. If the component around 6200 Å is Si II λ6355, its velocity in the first 2 days is slightly lower than that of He I λ6678. The variation of optical depth can account for this minor velocity difference. However, as time progresses, the velocity of this component decreases rapidly, clearly distinguishing it from other photospheric components. At $t \sim 16$ days, assuming that it is Si II λ6355, its velocity is only ~20% of that of He and Ca, making this absorption unlikely to be photospheric Si. This rapid decline in velocity aligns with the characteristics of high-velocity features consistent with the high-velocity Hα assumption. As shown in panels (c) and (d) of Figure 6, the assumption of Hα provides a better fit for the spectrum at $t \approx +6$ days compared to Si II λ6355. Therefore, we confirm that the absorption near 6200 Å is due to high-velocity Hα rather than Si IIλ6355 based on velocity evolution.

The higher velocity of Hα absorption compared to He I and Ca II suggests that it originates in the hydrogen at the outer layer of the ejecta. At $t \sim 16$ days, the velocity of Hα becomes comparable to that of other photospheric components, indicating an extensive distribution of hydrogen that spans both the outer and inner layers of the ejecta.

Through SNID fitting, we identified a sample group with early spectra similar to SN 2014C, as presented in Figure 8. These samples are classified as SNe Ib or SNe Ib/c in the literature. Generally, the spectra of SN 2014C are more similar to SN 2008D and iPTF 13bvn than other comparisons. They exhibit similarities in the profiles and evolutionary trends of He I line and high-velocity Hα. Their main differences are reflected in the velocity and width of the Ca II infrared triplet (IRT). SN 2014C exhibits a faster and narrower Ca II IRT velocity at $t \approx -7$ days, but around 2 weeks after maximum

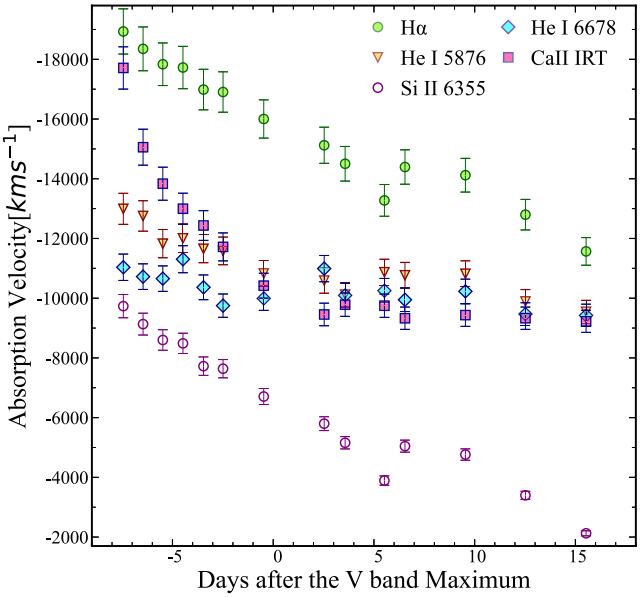

Figure 7. Evolution of line velocities for Hα, Si II λ6355, He I λ5876, He I λ6678, and the Ca II IR triplet of SN 2014C, derived from the absorption minima of each spectral line. Note: velocities of Hα and Si II λ6355 are derived from the same absorption line around 6200 Å.

light its Ca II IRT becomes stronger instead. Those reflect the similarities and differences in the ejecta structures of these SNe.

Notably, early high-velocity Hα components similar to SN 2014C are prevalent in the early stages of these SNe Ib/c. However, the high-velocity Hα absorption feature of SN 2014C persists for a relatively long duration, with significant absorption still evident at $t \sim 16$ days. In contrast, the corresponding absorption components in iPTF 13bvn, SN 2004gq, SN 2007C, and SN 2007Y diminish around 10 days after maximum light. The slower evolution of Hα in SN 2014C compared to these companions suggests a denser stripped H-rich envelope in SN 2014C relative to the other samples.

Figure 9 illustrates the velocities of He I λ5876, the strongest optical He I line in SN 2014C, and the comparison sample. He I lines result from nonthermal excitation and ionization of gamma-ray photons produced during the RD of ^{56}Ni and ^{56}Co (R. P. Harkness et al. 1987; L. B. Lucy 1991; P. A. Mazzali & L. B. Lucy 1998), revealing variations in the ejecta of SNe Ib, which exhibit a wide velocity range. The velocities of SN 2014C closely resemble those of SN 2008D, following a similar evolutionary trend to iPTF 13bvn, suggesting comparable ionization states and optical depths of the ejecta during the photospheric phase.

4.2. Nebular Phase

SNe typically become fully transparent around 100–200 days after maximum light, though some may take up to a year to complete this transition (P. A. Mazzali et al. 2004). During this period, the ejecta becomes optically thin, offering a clearer view of the explosion's core, a stage known as the nebular phase. In this phase, emission lines overlay the residual photospheric spectrum.

The right panel of Figure 3 displays five nebular spectra of SN 2014C taken from approximately $t \approx 98$ days to $t \approx 303$ days. These spectra are dominated by strong forbidden emission lines of intermediate-mass elements (e.g., [O I] λλ6300, 6364 and [Ca II] λλ7292, 7324). Unlike the narrow

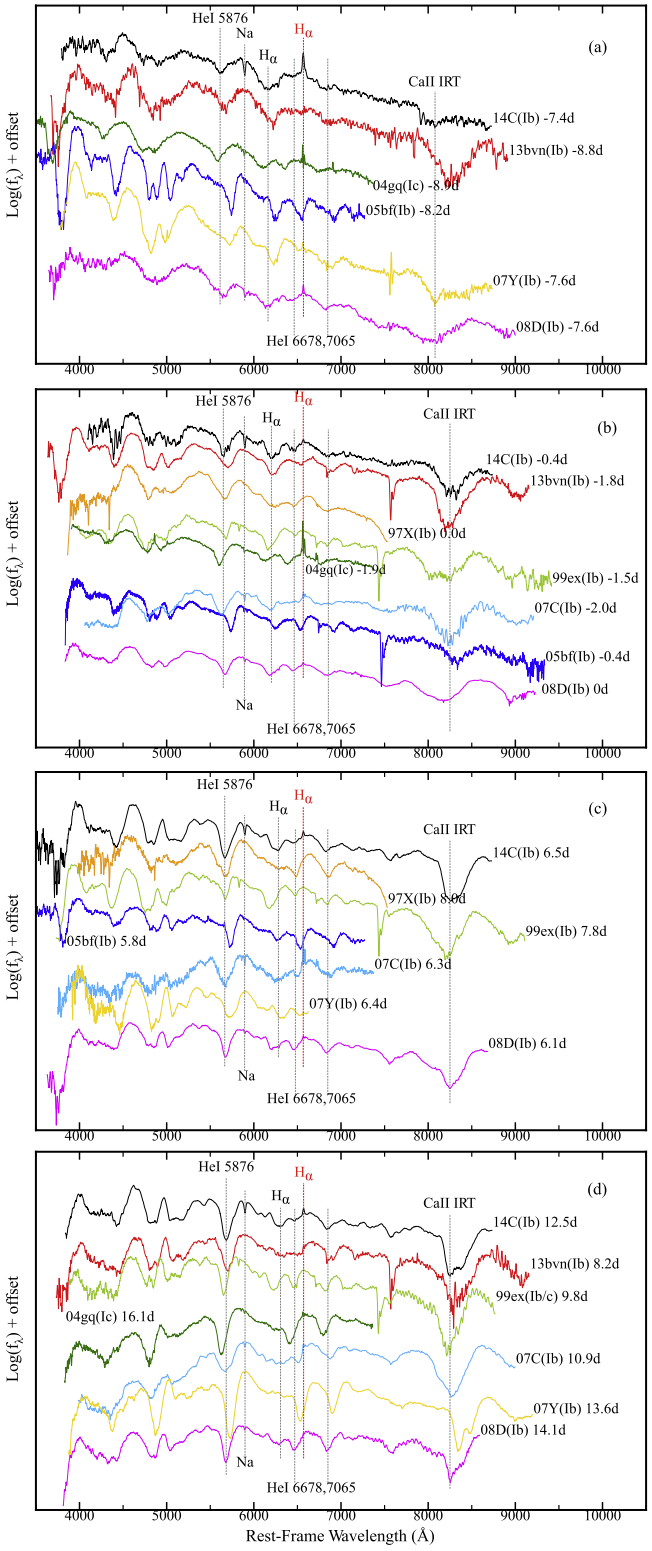

Figure 8. Comparison of spectra of SN 2014C with similar epoch spectra of other well-studied SNe. Labels in parentheses to the right of each spectrum indicate days from the *V*-band maximum time. References for each spectrum are listed in Table A6. These spectra have been corrected for redshift and reddening.

Hα observed in the early phase, stronger Hα emission with moderate width (e.g., ~1000 km s^{-1}) in the nebular spectra indicates significant SN−CSM interaction. This is observed

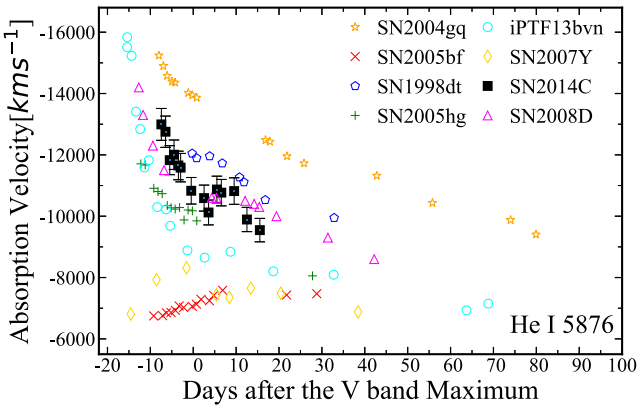

Figure 9. Velocity derived from the absorption minimum of He I λ5876, including SN 1998dt (T. Matheson et al. 2001); SN 2005bf (N. Tominaga et al. 2005); SN 2004gq, SN 2005hg, and SN 2008D (Figure 13 of M. Modjaz et al. 2009); iPTF 13bvn (C. Fremling et al. 2014); SN 2007Y (M. Stritzinger et al. 2009); and SN 2014C (this work).

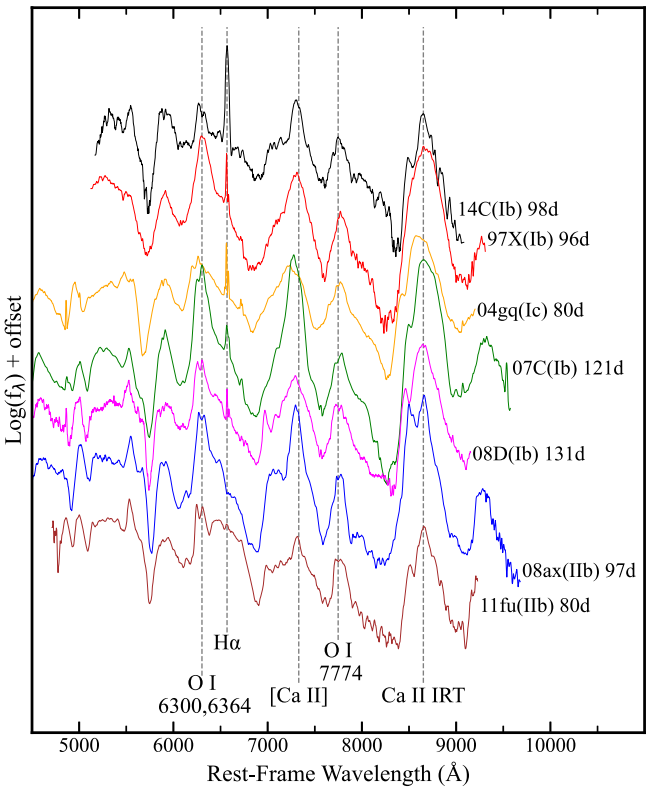

Figure 10. Comparison of nebular phase spectra of SN 2014C with other similar samples or well-studied SNe, including SN 1997X (S. Taubenberger et al. 2009), SN 2004gq (M. Modjaz et al. 2014), SN 2007C (S. Taubenberger et al. 2009), SN 2008D (M. Modjaz et al. 2009), SN 2008ax (S. Taubenberger et al. 2011), and SN 2011fu (A. Morales-Garoffolo et al. 2015). Labels in parentheses to the right of each spectrum indicate days from the *V*-band maximum time. These spectra have been corrected for redshift and reddening.

approximately 18 days earlier than reported by D. Milisavljevic et al. (2015). Given a velocity of ~10,000 km s^{-1}, the inner radius of the CSM is estimated to be ~10^{16} cm. The presence of strong hydrogen emission lines at this epoch suggests that the primary coolant might be the hydrogen of the stripped envelope (A. Uomoto & R. P. Kirshner 1986; C. Fransson & R. A. Chevalier 1987).

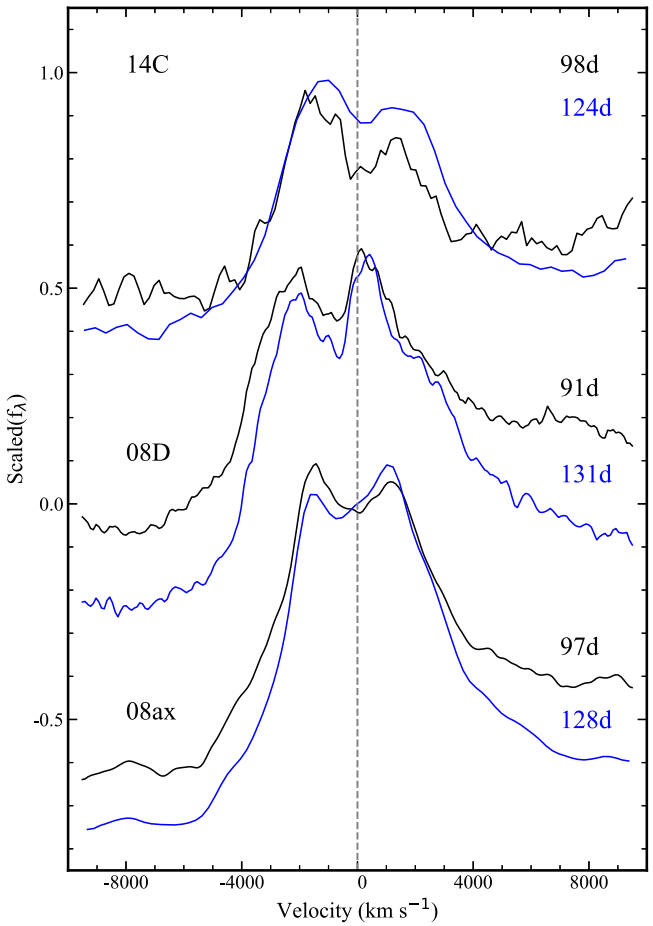

Figure 11. The emission lines of the [O I] $\lambda\lambda$6300, 6364 double peak of SN 2014C, SN 2008D (M. Modjaz et al. 2009), and SN 2008ax (R. Chornock et al. 2011; S. Taubenberger et al. 2011) in velocity space. The zero-point is 6300 Å and is indicated by the gray dashed line. These spectra were corrected for the redshift.

Figure 10 presents the nebular spectrum of SN 2014C at $t \approx 98$ days alongside spectra from some typical SNe Ib/c. The Hα emission line observed in the SN 1997X, SN 2004gq, SN 2007C, and SN 2008D spectra is mainly due to the background radiation. Notably, its intensity and width are significantly weaker compared to SN 2014C. In addition to its more pronounced Hα emission line, SN 2014C shares similar nebular traits with its counterparts, suggesting a similar core formed in these explosions. The observed SN Ib characteristics suggest that the CSM surrounding SN 2014C either was not highly opaque or featured a ring-like structure that allowed light to escape from the inner part of the SN.

At $t \approx 98$ days, SN 2014C shows double-peaked oxygen emission lines consistent with the comparisons except for SN 1997X. This is due to the intrinsic doublet of [O I] $\lambda\lambda$6300, 6364. We do not observe the double-peaked structure in [O I] λ7774 of SN 2014C, seen in SN 2007C and SN 2008D. This difference in oxygen profile relates to the structure of the ejecta. For example, the double-peaked [O I] λ7774 might suggest that the oxygen-rich ejecta are arranged within a ring- or torus-like structure viewed along the equatorial plane (P. A. Mazzali et al. 2005; K. Maeda et al. 2008; S. Taubenberger et al. 2009).

Figure 11 highlights the [O I] $\lambda\lambda$6300, 6364 emission lines for SN 2014C, SN 2008D, and SN 2008ax, showcasing differences in their intensities and velocities. Although the

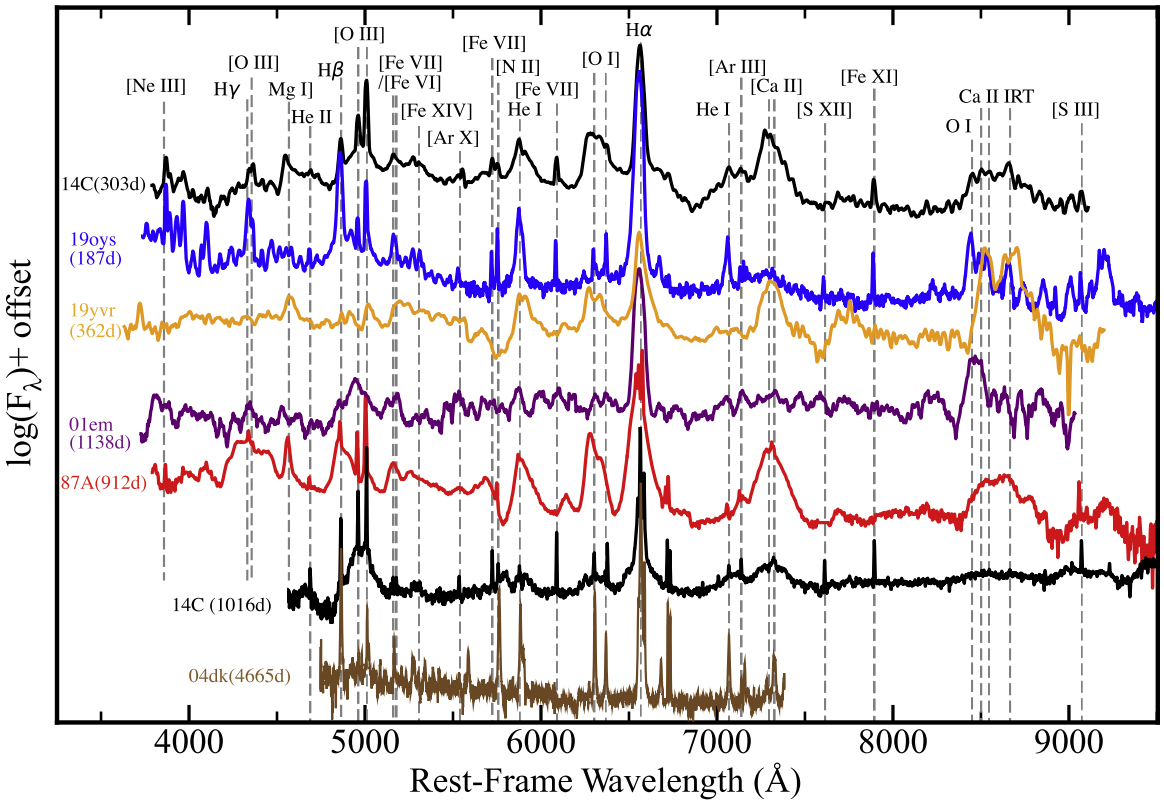

Figure 12. Spectra of SN 2014C at $t \sim 303$ days (this work) and $t \sim 1016$ days (I. Shivvers et al. 2019) compared to those of SN 2014C−like SN 2019oys (J. Sollerman et al. 2020), SN 2019yvr (L. Ferrari et al. 2024), SN 2001em (I. Shivvers et al. 2019), and SN 2004dk (J. C. Mauerhan et al. 2018) and SN II SN 1987A (from the Padova-Asiago database). Labels in parentheses to the left of each spectrum indicate days from the peak brightness. These spectra have been corrected for redshift and reddening. Various bin sizes were used for the different spectra, depending on the original signal-to-noise ratio.

intensities of the double peaks in SN 2014C and SN 2008ax are inconsistent, the positions of their respective double peaks relative to 6300 Å are essentially the same. This structure is classified as symmetric peaks in the study of [O I] line profiles by D. Milisavljevic et al. (2010). They suggested that the symmetric structure of the [O I] lines originates from the doublet produced by a single emitting source located at the front of the SN, moving toward the observer. Conversely, the double peaks of SN 2008D are asymmetrically distributed around 6300 Å, with the overall profile exhibiting a blueshift and the velocity of the [O I] λ6364 line nearing zero, indicating a difference in viewing angle or movement of the emitting source compared to SN 2014C.

The exhibition of intermediate Hα emission lines at $t \gtrsim 100$ days leads some to classify SN 2014C as an SN IIn. However, D. Milisavljevic et al. (2015) found that the spectra of SN 2014C at $t > 300$ days did not fully align with the nebular spectra of SNe IIn. For instance, the nebular spectra of SN 2014C have no broad emission component beneath the intermediate Hα emission line owing to H-rich ejecta, suggesting that its ejecta were H-poor at this time.

Figure 12 compares the spectra of SN 2014C at $t \approx 303$ and 1016 days with four metamorphic SNe from Type Ib to IIn, SN 2001em (I. Shivvers et al. 2019), SN 2004dk (J. C. Mauerhan et al. 2018), SN 2019oys (J. Sollerman et al. 2020), and SN 2019yvr (L. Ferrari et al. 2024), captured during the emergence of intermediate Hα emission from the SN−CSM interaction. Highly ionized narrow emission lines of Fe, Ar, S, and N seem to be common in these metamorphic SNe. Due to the limitations of spectral resolution, the widths of these narrow lines are often comparable to the instrumental broadening, suggesting that their intrinsic widths do not exceed 100 km s^{-1}, which is consistent with stellar wind velocities. This implies that these narrow emission lines may originate from the unshocked CSM (N. N. Chugai & R. A. Chevalier 2006).

The narrow lines of Hβ and [O III] $\lambda\lambda$4959, 5007 can easily be mistaken for radiation from the galactic background. However, in the case of SN 2014C, these lines are superimposed on a broader profile. This resembles the scenario where narrow emission lines generated by photoionization in SN−CSM interactions are superimposed on broad emission lines produced by electron scattering (L. Dessart et al. 2017). During 7 yr spectral monitoring, B. P. Thomas et al. (2022) observed the evolution of the intensity of these two [O III] lines. Therefore, these narrow lines are likely to originate from interactions rather than the galactic background.

At $t \approx 303$, the notable Type Ib components in SN 2014C, e.g., emissions of [O I], [Ca II], and Ca II IRT at the width of ~3000 km s^{-1}, indicates that the energy from the SN still contributed to the observed luminosity, although this contribution was progressively diminishing. Subsequently, at $t \gtrsim 330$ days, the typical Type Ib emission lines gradually weakened in SN 2014C; only weak [Ca II] and [O I] emission lines were observable, with most other spectral features being produced by SN−CSM interactions (J. C. Mauerhan et al. 2018). At $t > 1200$ days, the Type Ib components were almost undetectable in the spectrum, primarily due to the extremely low luminosity of the SN itself (B. P. Thomas et al. 2022).

Like SN 2014C, the spectrum of SN 2019oys at $t \approx 187$ days exhibits narrow emission lines from highly ionized elements

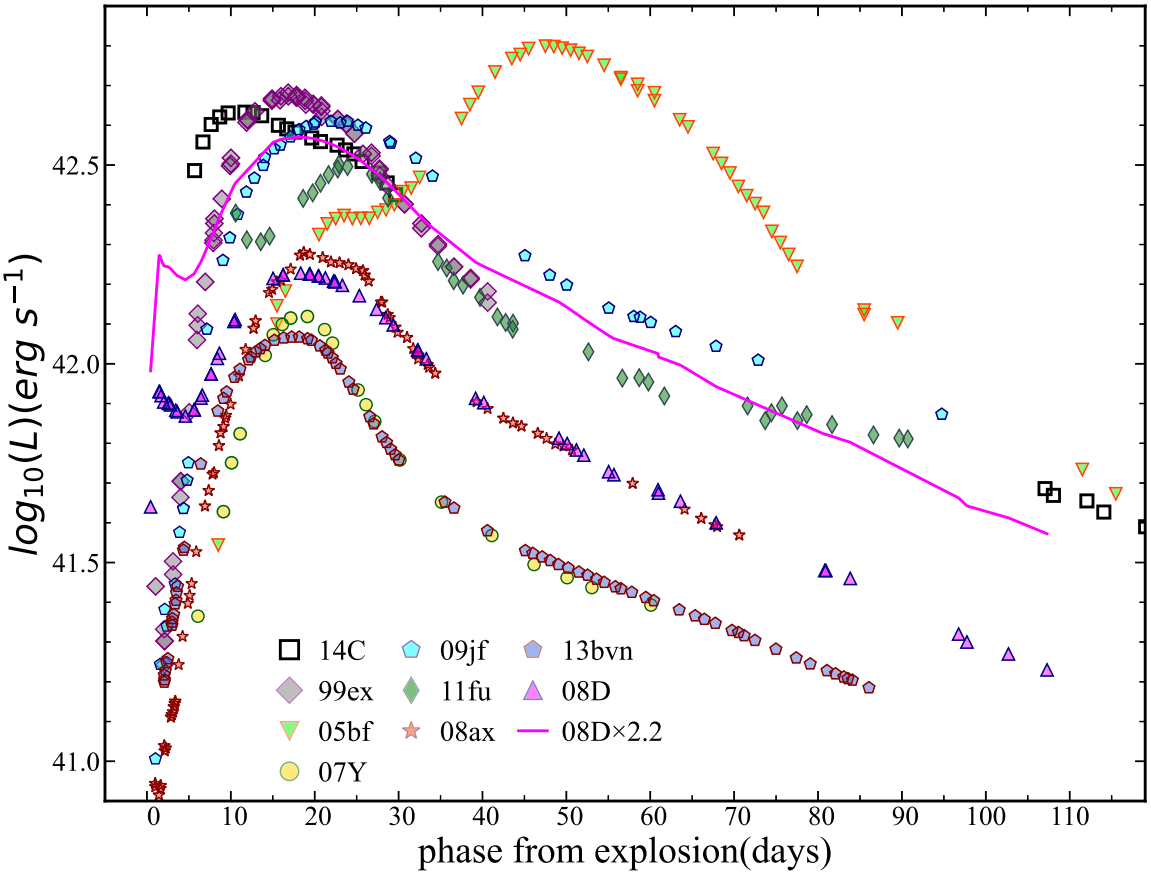

Figure 13. The bolometric light curve of SN 2014C compared with some well-studied SESNe, including SNe IIb SN 2008ax (A. Pastorello et al. 2008) and SN 2011fu (B. Kumar et al. 2013); SN IIb/Ib SN 2007Y (M. Stritzinger et al. 2009); SNe Ib SN 1999ex (M. Stritzinger et al. 2002), SN 2008D (P. A. Mazzali et al. 2008; D. Malesani et al. 2009a), SN 2009jf (S. Valenti et al. 2011), and iPTF 13bvn (C. Fremling et al. 2014); and SN Ib/c SN 2005bf (G. Folatelli et al. 2006). The light curve of SN 2008D scaled by a factor of 2.2 is plotted with a solid line.

such as Fe, Ne, and Ar. However, the [Ca II] emission lines in SN 2019oys are significantly fainter than those in SN 2014C at $t \approx$ 303 days, and the Ca II IRT lines of the former are relatively weak. Additionally, the [O I] $\lambda\lambda$6300, 6364 emissions in SN 2019oys are as narrow as seen in the spectrum of SN 2014C at $t \approx 1016$ days, lacking the broadening typically seen in SNe Ib at about 200 days after the explosion, suggesting that its oxygen emission originates primarily from CSM rather than the SN itself. The broad emission lines of O and Ca disappeared or became very weak in the spectrum of SN 2019oys, indicating that the outer CSM heavily obscured the inner region of this SN. Thus, the CSM of SN 2109oys has a significantly different optical depth or structure from that of SN 2014C.

SN 2019yvr exhibits broad lines of Ca, O, and H akin to SN 2014C, yet it lacks the narrow emission lines typical of highly ionized species, such as Fe and Ne. This suggests that, at this stage, the SN core of SN 2019yvr is comparable to that of SN 2014C, but its outer CSM differs.

The first interaction spectrum of SN 2001em, dominated by intermediate Hα emission, was observed around 1000 days post-explosion. Due to the low signal-to-noise ratio, no narrow emission lines originating from highly ionized species of Fe, Ar, and O were discernible in this spectrum. Therefore, it is unclear whether its CSM shares a similar composition and ionization state with SN 2014C and SN 2019oys. The relatively weak broad Ca and O emissions imply that the contribution of SN was weaker than the SN−CSM interaction, as observed in SN 2014C at the same phase.

Over 4000 days after the explosion, the first spectrum capturing the interaction between SN 2004dk and its CSM was obtained. By this time, the brightness of SN had diminished, allowing the spectrum to be dominated by intermediate Hα emission and narrow ionized lines from elements like He, N, Ar, and Fe. Similar to SN 2014C and SN 2019oys, SN 2004dk showed [Fe VII] λ5158 but did not exhibit [Fe VII] $\lambda\lambda$5720, 6087, suggesting similar yet distinct CSM characteristics among these SNe.

Through comparison of Figure 12, we found that the spectrum of SN 2014C at $t \approx 303$ days is more similar to that of the SN II SN 1987A at $t \approx 912$ days. However, the broad Hα and Hβ emissions in the spectrum of SN 1987A, comparable to those of [O I] and [Ca II], more likely originate from the SN itself than from the SN−CSM interaction. Furthermore, SN 1987A exhibits narrow ionized emission lines such as [Ne III], [O III], and He II but lacks highly ionized Fe lines, highlighting significant differences in CSM composition compared to SN 2014C. SN 1987A originated from the explosion of a blue supergiant (W. D. Arnett et al. 1989), a H-rich star that differs significantly from the typical progenitor of SNe Ib/c. Therefore, the differences in the narrow components of its spectrum compared to SN 2014C are likely related to the mass-loss processes in the final stages of their progenitor system.

In brief, although the nebular spectra of these SNe presented in Figure 12 share many similarities with those of SN 2014C,

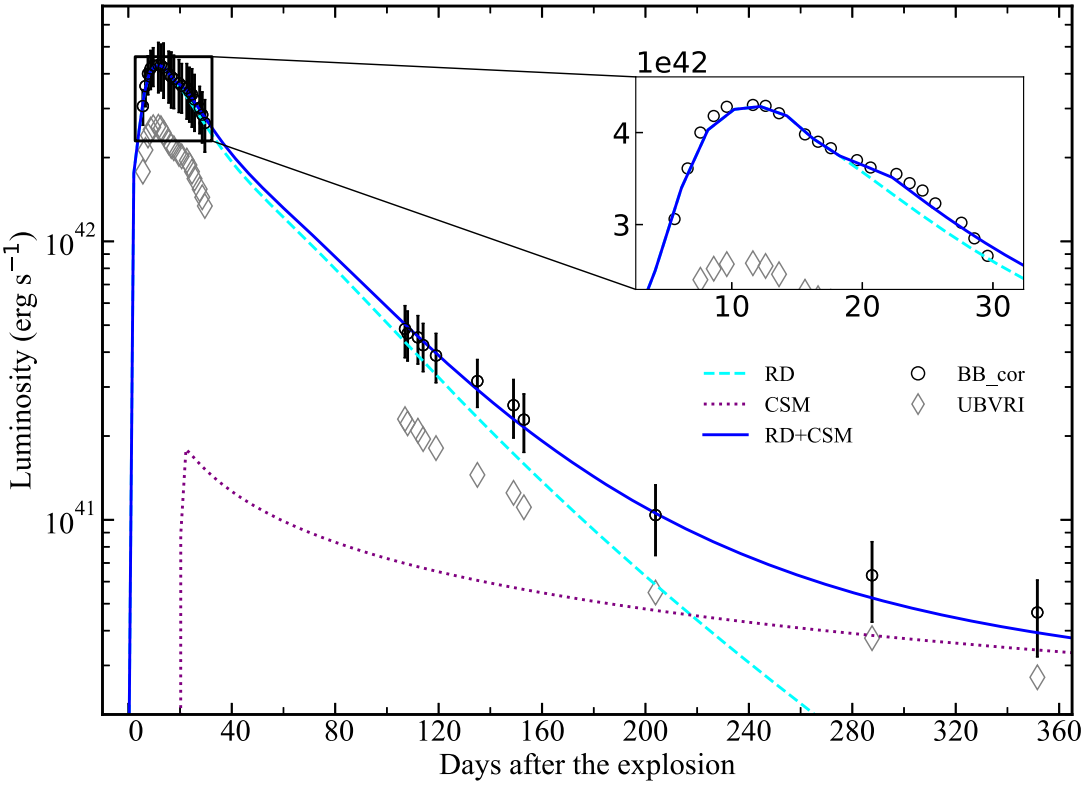

Figure 14. Bolometric light curve of SN 2014C derived from the blackbody fit based on the *UBVRI*-band photometry. The integrated flux of the *UBVRI* bands is also plotted. The dotted, dashed, and solid lines represent the RD, CSM, and RD+CSM models, respectively.

there are also notable differences. These discrepancies may be related to the transparency, composition, and structure of CSM, or the properties of explosion productions. Ultimately, they can be attributed to the different envelope-stripping processes of the progenitor before the explosion.

5. Bolometric Light Curve and Modeling

Figure 13 presents the bolometric light curve of SN 2014C derived from the blackbody fitting of *UBVRI*-band photometry. The peak bolometric luminosity of SN 2014C, $L_{\rm max} \approx 4.3 \times 10^{42}$erg s^{-1}, is higher than typical SN Ib values (e.g., ~1.5×10^{42} erg s^{-1}; L. Dessart et al. 2020), with a rise time of ~11.6 days, shorter than the usual ~20 days for SNe Ib. Even within the SESN family, the peak luminosity of SN 2014C remains on the high side. This figure compares it with a representative group of SESNe, showing that the peak luminosity of SN 2014C is comparable to that of SN Ib 1999ex and only lower than that of SN Ib/c SN 2005bf. The exceptional luminosity of SN 2005bf could be attributed to the energy supplied by a magnetar resulting from the explosion, given that this SN may be associated with a gamma-ray burst (G. Folatelli et al. 2006).

The bolometric luminosity of SN 2008D, when scaled by a factor of 2.2, aligns closely with that of SN 2014C during 15 days $\lesssim \tau \lesssim$ 30 days. For $\tau \gtrsim$ 30 days, the luminosity evolution of SN 2014C may initially follow a trend similar to that of SN 2008D but subsequently decreases at a slower rate. This partially fills the data gap for SN 2014C between 30 days $\lesssim \tau \lesssim$ 100 days. Considering the uncertainty in the explosion time of SN 2014C, if we assume that it reached its bolometric peak around 20 days, similar to SN 2008D, this could explain the similarity in their spectral features, particularly the velocity evolution of He I λ5876. However, even with this amplification factor, the luminosity of SN 2014C remains significantly higher than that of SN 2008D both before the peak and during the tail phase.

Following the RD model (e.g., Arnett law; W. D. Arnett 1982; M. Stritzinger & B. Leibundgut 2005), as seen in Equation (1), the mass of ^{56}Ni produced during the explosion is $M(^{56}\mathrm{Ni}) = 0.14 \pm 0.03\,M_{\odot}$,

$$M_{\rm Ni} = \frac{L_{\rm max}}{10^{43}\ {\rm erg\ \ s^{-1}}} \times (6.45e^{-\frac{t_r}{\tau_{\rm Ni}}} + 1.45e^{-\frac{t_r}{\tau_{\rm Co}}})^{-1}, \quad (1)$$

where $\tau_{\rm Ni} = 8.8$ days and $\tau_{\rm Co} = 111.3$ days are the decay times of ^{56}Ni and ^{56}Co, respectively. This result aligns with the estimate by R. Margutti et al. (2017), who calculated 0.15 $M_{\odot}$, accounting for their 0.2 mag overestimation in peak luminosity.

As shown in Figure 14, the bolometric light curve of SN 2014C at $\tau \lesssim$ 15 days can be well fitted by the RD model with $M(^{56}\mathrm{Ni}) = 0.14\ M_{\odot}$. This suggests that SN 2014C could be mainly powered by RD during the early phase. The fast rise could be attributed to a small progenitor radius or a relatively high ratio of explosion energy to ejected mass. However, SN 2014C exhibits flux excess at $\tau \gtrsim 20$ compared to this model, indicating the presence of an additional energy source apart from the RD of ^{56}Ni.

The flat and blue color curve seen in Figure 5 at $\tau \gtrsim 20$, along with the absence of significant X-ray emissions during the first 20 days (R. Margutti et al. 2017), supports the hypothesis of delayed interaction between the SN and surrounding CSM. Previous observational evidence suggests that the interaction of SN 2014C began 45 days post-explosion and continued for more than 2000 days (D. Milisavljevic et al. 2015; S. Tinyanont et al. 2016; G. E. Anderson et al. 2017;

R. Margutti et al. 2017; D. Brethauer et al. 2022; B. P. Thomas et al. 2022). Therefore, a hybrid model incorporating both RD and ejecta−CSM interaction (CSIRD) is adopted to explain the light curve of SN 2014C.

Assume that the CSM has a stellar wind density profile (i.e., $\rho \propto r^{-2}$) and that the density of SN ejecta is uniform for the inner ejecta and follows $\rho \propto r^{-n}$ (here $n = 7$) for the outer ejecta with the dimensionless transition radius of $x_0 = 0.3$. Here we develop the popular CSMRD model (E. Chatzopoulos et al. 2012, 2013) by introducing a gamma-ray leakage factor of $A \approx 3n(n-3)x_0\kappa_{\rm Ni}M_{\rm ej}/[4\pi(n-1)(n-3+3x_0^3)v_{\rm ej}^2]$ ($x_0^n << 1$). The modified CSMRD-powered luminosity can be rewritten as

$$L_{\rm SN} = \frac{1}{t_0}\exp^{-t'/t_0}\int_0^t \exp^{t'/t_0}P_{\rm CSI\,inp}dt' + \frac{1}{t'_0}\exp^{-t'/t'_0}\int_0^t \exp^{t'/t'_0}P_{\rm RD\,inp}(1-\exp^{-At'^{-2}})dt', \quad (2)$$

where t_0 and t'_0 are the diffusion timescales through the total CSM mass ($M_{\rm CSM}$) and the CSM+SN mass ($M_{\rm CSM} + M_{\rm ej}$), $P_{\rm CSI,inp}$ and $P_{\rm Ni,inp}$ are the input powers from the ejecta−CSM interaction (E. Chatzopoulos et al. 2012) and RD of ^{56}Ni + ^{56}Co (S. Valenti et al. 2008), and $\kappa_\gamma = 0.027\,{\rm cm^2\,g^{-1}}$ is the opacity to the gamma-ray photons from ^{56}Ni and ^{56}Co decay (e.g., E. Cappellaro et al. 1997; P. A. Mazzali et al. 2000; K. Maeda et al. 2003; Z. G. Dai et al. 2016). The detection of interaction signals starting 20 days post-explosion indicates that the SN ejecta caught up with the H-rich CSM at that moment. Hence, we set the prior on the initial time of interaction as $t_i = 20 \pm 5$ days. The CSM mass is set to be 1 $M_\odot$, as inferred from X-ray and radio observations (D. Milisavljevic et al. 2015; R. Margutti et al. 2017). Factors affecting the final fitting results, such as the structure of CSM and the efficiency of converting kinetic energy into radiation during the SN−CSM interaction, were not fully accounted for in this study. We used a spherically symmetric CSM structure rather than more complex configurations, such as the torus-shaped CSM proposed by B. P. Thomas et al. (2022). This simplification may lead to an overestimation of CSM mass (D. Brethauer et al. 2022). However, S. Orlando et al. (2024) utilized 3D hydrodynamic modeling to determine a CSM mass of 2.5 $M_\odot$ for SN 2014C, which exceeds the values reported in most recent research. Considering the uncertainties in CSM mass estimation, our intermediate value is deemed appropriate.

Based on a Markov Chain Monte Carlo (MCMC) sampling algorithm (D. Foreman-Mackey et al. 2013), the fitting with the CSIRD model suggests that the SN ejecta has a total mass of $2.22^{+0.69}_{-0.77}\,M_\odot$ and a ^{56}Ni mass of $0.14^{+0.01}_{-0.01}\,M_\odot$, and more details are presented in Figure 15. The CSM has an inner-radius density of $(1.81^{+1.57}_{-0.78}) \times 10^{-14}\,{\rm g\,cm^{-3}}$, and the initial time of interaction is $t_i = 19.9^{+3.34}_{-3.25}$ days. The efficiency of interaction energy converted to radiation is $0.2^{+0.3}_{-0.1}$. If the CSM results from a mass ejection of the progenitor star before the explosion, the mass-loss rate can be estimated as $0.2/(v_{\rm CSM}/1000\,{\rm km\,s^{-1}})\,M_\odot\,{\rm yr^{-1}}$, where $v_{\rm CSM}$ is the velocity of the CSM. Wolf−Rayet stars or red supergiant stars have difficulty in producing such intense ejections, while giant eruptions from a luminous blue variable star (LBV) can be responsible for such violent pre-SN mass ejection of 10^{-2} to $10\,M_\odot\,{\rm yr^{-1}}$ (see N. Smith 2014; K. Bhirombhakdi et al. 2019, and references therein). Given the complex CSM revealed by our observations and the progenitor observation (N.-C. Sun et al. 2020), SN 2014C could originate from the explosion of an LBV in a binary system.

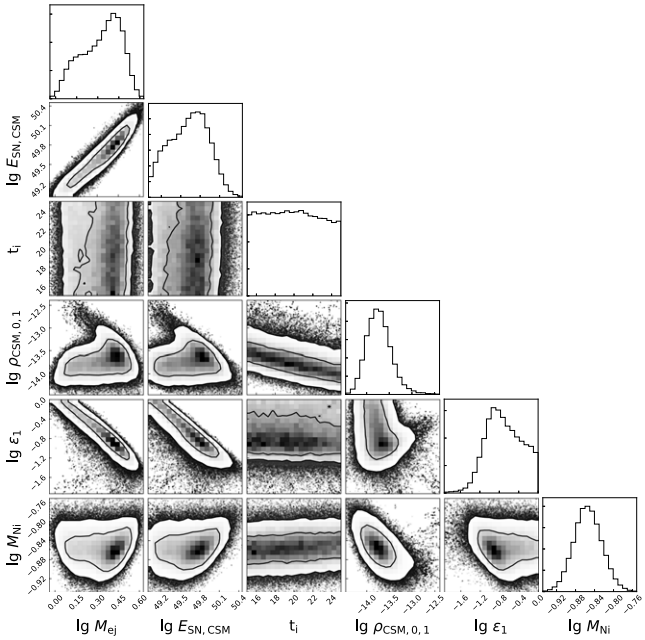

Figure 15. Joint confidence level contours of the CSIRD parameters inferred from the MCMC-based fitting.

6. Summary

This work presents high-cadence spectral and photometric observations of SN 2014C during the first month after its explosion. We achieved precise photometric results using the template subtraction method, while the analysis of over 10 early spectra revealed detailed insights into ejecta evolution. These observations, along with related calculations and model analyses, improve the understanding of the nature of this metamorphic SN.

The light curve of SN 2014C exhibited a faster rise time (~11.5 days) than typical SNe Ib/c ($\gtrsim$16 days) and reached a relatively higher peak luminosity ($L_{\rm max} \approx 4.3 \times 10^{42}\,{\rm erg\,s^{-1}}$). The rapid rising luminosity could indicate a high ratio of explosion energy to ejecta mass. Based on the peak luminosity, we estimate that this SN synthesized $0.14\,M_\odot$ of ^{56}Ni during the explosion. However, the energy released from the RD of this nickel is still insufficient to fully account for the light curve at $\tau \gtrsim 20$ days. To address this, we introduced an SN−CSM interaction model to provide additional energy. Although this combined model fits the observed data reasonably well, it is important to acknowledge that it represents only one possible explanation. The SN−CSM interaction could have commenced earlier and intensified rapidly, leading to the swift rise in the light curve and influencing the peak luminosity. Consequently, the nickel mass derived from the peak bolometric luminosity may represent an upper limit, suggesting that the amount of nickel synthesized could be lower.

The decelerating and fading Hα absorption, observed at a velocity higher than those of the photospheric components like

Ca and He at $t \lesssim 16$ days, indicates that the hydrogen envelope of the progenitor was not completely stripped before the core collapse.

Through the earliest interaction signal detected in the photometry, the presence of CSM begins at a distance of 4×10^{14} cm from the SN. However, factors such as density or optical depth prevented the observation of significant SN −CSM interaction signals in the spectrum during this phase. The emergence of intermediate Hα at $t \approx 98$ days suggests a denser CSM located at $\sim 10^{16}$ cm. These observations imply variations in the CSM, as reported by R. Margutti et al. (2017). They found that the CSM had a low density at $R \lesssim 2 \times 10^{16}$ cm and the dense H-rich material region at $R \sim 5.5 \times 10^{16}$ cm. Furthermore, the very long baseline interferometry observations have revealed a circular thin spherical shell as the structure of the H-rich CSM (M. F. Bietenholz et al. 2018, 2021; B. P. Thomas et al. 2022), and the CSM contains a mixture of carbonaceous and silicate and extends to at least 1.4×10^{17} cm (S. Tinyanont et al. 2019).

Given the presence of a small amount of hydrogen in the envelope and the nearby H-rich CSM with varying densities, it is evident that SN 2014C originated in a highly complex H-rich environment. This complex environment may be responsible for translating characteristics of SN 2014C among those of SNe Ib, IIb, and IIn. The transitional behavior of SN 2014C suggests that massive stars can explode at any phase during envelope stripping, and the state of stripping and the surrounding environment at the time of explosion contribute to the rich diversity observed in SESNe.

Acknowledgments

We thank the anonymous referee for providing a comprehensive report clarifying the paper and sparking fresh, qualitative insights. This work is supported by the National Key R&D Program of China with No. 2021YFA1600404, the National Natural Science Foundation of China (12173082, 12333008), the science research grants from the China Manned Space Project with No. CMS-CSST-2021-A12, the Yunnan Fundamental Research Projects (grants 202401BC070007 and 202201AT070069), the Top-notch Young Talents Program of Yunnan Province, the Light of West China Program provided by the Chinese Academy of Sciences, and the International Centre of Supernovae, Yunnan Key Laboratory (No. 202302AN360001). E.P. is grateful to INAF for financial support.

We acknowledge the support of the staff of the LJT, the Asiago Copernico 1.82 m telescope, and NOT. Funding for the LJT has been provided by the CAS and the People's Government of Yunnan Province. The LJT is jointly operated and administrated by YNAO and the Center for Astronomical Mega-Science, CAS.

Facilities: YAO:2.4m, Swift, Asiago:Copernico, NOT.

Software: PyRAF (Science Software Branch at STScI 2012), NumPy (C. R. Harris et al. 2020), Matplotlib (J. D. Hunter 2007), Astropy (Astropy Collaboration et al. 2013, 2018, 2022).

Appendix
Photometric and Spectroscopic Data

Table A1 enumerates the standard *UBVRI* magnitudes for 12 local reference stars calibrated against the Landolt luminosity stars. Utilizing these reference stars, the instrumental magnitudes captured by the LJT for SN 2014C were transformed into standard *UBVRI* magnitudes, as detailed in Table A2. The photometric outcomes from Swift-UVOT are summarized in Table A3. The log of spectroscopic observations for SN 2014C, conducted in 2014, is outlined in Table A4. The photometric parameters of the sample presented in Figures 4 and 5 are collected in Table A5. Lastly, the reference list for Figure 8 is provided in Table A6.

Table A1
Photometry of the Comparison Stars in the Field of SN 2014C[a]

Star	R.A.	Decl.	*U* (mag)	*B* (mag)	*V* (mag)	*R* (mag)	*I* (mag)
1	22:37:12.236	+34:28:49.74	16.51(0.02)	16.41(0.01)	15.72(0.01)	15.34(0.01)	14.93(0.01)
2	22:37:13.729	+34:28:27.68	17.64(0.03)	17.13(0.01)	16.25(0.01)	15.77(0.01)	15.30(0.01)
3	22:37:11.107	+34:27:29.33	17.48(0.01)	17.31(0.01)	16.61(0.01)	16.24(0.01)	15.83(0.01)
4	22:36:53.994	+34:27:19.53	16.57(0.02)	16.42(0.02)	15.73(0.01)	15.37(0.01)	14.98(0.01)
5	22:37:20.518	+34:25:15.85	17.10(0.02)	16.67(0.01)	15.82(0.01)	15.35(0.01)	14.90(0.01)
6	22:37:16.932	+34:24:28.56	18.12(0.03)	17.51(0.01)	16.62(0.01)	16.16(0.01)	15.71(0.01)
7	22:37:22.365	+34:24:19.10	17.55(0.02)	16.68(0.01)	15.68(0.01)	15.12(0.01)	14.58(0.01)
8	22:37:13.519	+34:23:24.97	16.76(0.03)	16.67(0.02)	15.96(0.01)	15.57(0.01)	15.16(0.01)
9	22:37:21.993	+34:23:21.52	18.58(0.02)	17.75(0.02)	16.70(0.01)	16.07(0.01)	15.42(0.01)
10	22:37:14.596	+34:23:07.57	16.44(0.03)	16.47(0.01)	15.89(0.01)	15.56(0.01)	15.20(0.01)
11	22:37:18.447	+34:22:48.35	17.31(0.01)	16.80(0.01)	15.93(0.01)	15.48(0.01)	15.03(0.01)
12	22:36:58.213	+34:22:05.50	17.45(0.01)	17.01(0.02)	16.12(0.01)	15.67(0.01)	15.22(0.01)

Note.
[a] See Figure 1 for the finder chart of these reference stars. *UBVRI* bands in the Vega magnitude system. Uncertainties (in parentheses) are 1σ.

Table A2
LJT *UBVRI*-band Photometry of SN 2014C[a] in 2014

Date (UT)	MJD	Epoch[b] (days)	*U* (mag)	*B* (mag)	*V* (mag)	*R* (mag)	*I* (mag)
Jan 7	56664.53	−5.44	16.72(0.02)	16.44(0.01)	15.44(0.01)	14.92(0.01)	14.45(0.01)
Jan 8	56665.53	−4.44	16.59(0.03)	16.24(0.01)	15.24(0.01)	14.71(0.01)	14.26(0.01)
Jan 8[c]	56665.81	−4.16	...	16.18(0.02)	15.13(0.03)	14.65(0.02)	...
Jan 9	56666.51	−3.46	16.56(0.03)	16.10(0.01)	15.10(0.01)	14.58(0.01)	14.08(0.01)
Jan 10	56667.53	−2.44	16.59(0.03)	16.08(0.01)	15.03(0.01)	14.48(0.01)	13.98(0.01)
Jan 11	56668.53	−1.44	16.63(0.03)	16.09(0.01)	14.99(0.01)	14.42(0.01)	13.90(0.01)
Jan 13	56670.53	0.56	16.94(0.04)	16.13(0.01)	14.94(0.01)	14.33(0.01)	13.84(0.04)
Jan 14	56671.50	1.53	16.92(0.03)	16.17(0.01)	14.95(0.01)	14.35(0.01)	13.80(0.01)
Jan 15	56672.53	2.56	17.16(0.07)	16.21(0.01)	14.98(0.01)	14.36(0.01)	13.79(0.01)
Jan 17	56674.52	4.55	17.26(0.03)	16.37(0.01)	15.06(0.01)	14.42(0.01)	13.80(0.01)
Jan 18	56675.52	5.55	17.38(0.02)	16.41(0.01)	15.09(0.01)	14.43(0.01)	13.82(0.01)
Jan 19	56676.50	6.53	17.36(0.03)	16.43(0.03)	15.12(0.01)	14.45(0.01)	13.83(0.01)
Jan 21	56678.50	8.53	17.43(0.05)	16.49(0.01)	15.16(0.01)	14.52(0.01)	13.84(0.01)
Jan 22	56679.54	9.57	17.41(0.03)	16.53(0.01)	...	...	...
Jan 24	56681.52	11.55	17.57(0.03)	16.57(0.01)	15.24(0.01)	14.54(0.01)	13.88(0.01)
Jan 25	56682.53	12.56	17.62(0.03)	16.63(0.02)	15.29(0.01)	14.56(0.01)	13.90(0.01)
Jan 26	56683.52	13.55	17.79(0.03)	16.72(0.03)	15.35(0.01)	14.59(0.01)	13.91(0.01)
Jan 27	56684.50	14.53	17.87(0.08)	16.81(0.02)	15.43(0.01)	14.63(0.01)	13.94(0.01)
Jan 29	56686.50	16.53	...	16.95(0.03)	15.55(0.01)	14.71(0.01)	13.96(0.01)
Jan 30	56687.49	17.52	18.04(0.13)	17.01(0.03)	...	...	14.02(0.01
Jan 31	56688.50	18.53	18.12(0.09)	17.06(0.06)	15.72(0.01)	14.86(0.01)	14.10(0.01)
Apr 18	56765.91	95.94	20.23(0.19)	19.18(0.09)	17.60(0.03)	16.68(0.03)	15.94(0.03)
Apr 19	56766.91	96.94	20.21(0.17)	19.21(0.12)	...	...	...
Apr 23	56770.90	100.93	...	...	17.73(0.03)	16.77(0.03)	15.99(0.03)
Apr 25	56772.92	102.95	...	...	17.82(0.04)	...	16.06(0.02)
Apr 30	56777.90	107.93	...	19.48(0.08)	17.88(0.04)	16.93(0.03)	16.16(0.04)
May 16	56793.90	123.93	20.79(0.12)	19.79(0.12)	18.14(0.03)	17.16(0.04)	16.38(0.03)
May 30	56807.88	137.91	...	...	18.29(0.04)	17.26(0.03)	16.68(0.03)
Jun 3	56811.89	141.92	...	...	18.42(0.05)	17.39(0.03)	16.81(0.03)
Jul 24	56862.80	192.83	21.88(0.24)	20.84(0.15)	19.18(0.08)	18.08(0.04)	17.78(0.11)
Oct 16	56946.54	276.57	...	...	19.39(0.08)	18.55(0.06)	18.48(0.09)
Nov 11[d]	56972.99	303.02	...	...	19.60(0.04)	18.63(0.04)	...
Dec 19	57010.48	340.51	...	...	19.88(0.26)	18.85(0.09)	18.78(0.12)

Notes.
[a] Uncertainties (in parentheses) are 1σ.
[b] The epoch is relative to the *V*-band maximum date, MJD = 56669.97.
[c] Photometry taken by Asiago 1.82 m telescope +AFOSC.
[d] Photometry taken by NOT+ALFOSC.

Table A3
Swift-UVOT Photometry of SN 2014C[a] in 2014

Date (UT)	MJD	Epoch[b] (days)	*uvw*1 (mag)	*u* (mag)	*b* (mag)	*v* (mag)
Jan 6	56663.25	−6.72	...	17.07(0.16)	17.01(0.14)	15.79(0.12)
Jan 7	56664.21	−5.76	18.62(0.26)	17.22(0.16)	16.73(0.11)	15.59(0.10)
Jan 9	56666.49	−3.48	18.82(0.21)	16.65(0.11)	16.11(0.08)	15.08(0.07)
Jan 9	56666.52	−3.45	...	...	16.06(0.07)	15.10(0.07)
Jan 11	56668.45	−1.52	...	16.85(0.12)	16.09(0.08)	14.96(0.07)
Jan 11	56668.54	−1.43	18.90(0.23)	16.84(0.12)	16.04(0.07)	14.93(0.08)
Jan 13	56670.44	0.47	19.00(0.25)	17.03(0.13)	16.04(0.07)	14.93(0.06)
Jan 14	56671.46	1.49	...	...	16.06(0.07)	14.97(0.06)
Jan 15	56672.43	2.46	...	17.29(0.15)	16.16(0.08)	14.93(0.06)
Jan 15	56672.91	2.94	19.24(0.29)	16.93(0.12)	16.11(0.08)	15.05(0.07)
Jan 17	56674.35	4.38	...	17.33(0.16)	16.26(0.08)	15.06(0.07)
Jan 18	56675.10	5.13	19.75(0.44)	17.40(0.16)	16.35(0.08)	15.14(0.07)
Jan 19	56676.24	6.27	...	17.57(0.18)	16.48(0.09)	15.10(0.07)
Jan 19	56676.50	6.53	19.49(0.35)	17.37(0.16)	16.39(0.08)	...

Notes.
[a] Uncertainties (in parentheses) are 1σ.
[b] The epoch is relative to the *V*-band maximum date, MJD = 56669.97.

Table A4
Journal of Spectroscopic Observations of SN 2014C in 2014

Date (UT)	MJD	Epoch[a] (days)	Range (Å)	Disp. (Å pixel^{-1})	Slit Width (pixels)	Exp. Time (s)	Air Mass	Telescope+Instrument
Jan 5	56662.53	−7.44	3800–8750	2.85	6.36	1800	1.54	LJT+YFOSC(G3)
Jan 6	56663.51	−6.46	3900–8750	2.85	6.36	2700	1.36	LJT+YFOSC(G3)
Jan 7	56664.49	−5.48	3550–8750	2.85	6.36	2700	1.26	LJT+YFOSC(G3)
Jan 8	56665.49	−4.48	3600–8750	2.85	6.36	2700	1.27	LJT+YFOSC(G3)
Jan 8	56666.28	−3.69	3370–8150	4.84	3.25	1800	1.48	1.82m+AFOSC(G4)
Jan 9	56666.51	−3.46	3600–8750	2.85	6.36	2700	1.45	LJT+YFOSC(G3)
Jan 10	56667.48	−2.49	5240–9200	1.50	6.36	3600	1.28	LJT+YFOSC(G8)
Jan 12	56669.50	−0.47	4100–8750	2.85	6.36	2700	1.40	LJT+YFOSC(G3)
Jan 13	56670.49	0.52	5830–8120	0.84	3.53	2700	1.35	LJT+YFOSC(E13)
Jan 15	56672.50	2.53	3900–8750	2.85	6.36	1800	1.48	LJT+YFOSC(G3)
Jan 16	56673.54	3.57	4100–8750	2.85	6.36	1800	1.99	LJT+YFOSC(G3)
Jan 18	56675.49	5.52	3500–8750	2.85	6.36	1800	1.45	LJT+YFOSC(G3)
Jan 19	56676.51	6.54	3490–8750	2.85	6.36	1800	1.68	LJT+YFOSC(G3)
Jan 22	56679.51	9.54	3500–8750	2.85	6.36	2100	1.75	LJT+YFOSC(G3)
Jan 25	56682.49	12.52	3750–8750	2.85	6.36	2400	1.69	LJT+YFOSC(G3)
Jan 28	56685.50	15.53	3800–8750	2.85	6.36	2333	1.91	LJT+YFOSC(G3)
Apr 20	56767.89	97.92	5180–9100	3.66	6.36	1500	1.92	LJT+YFOSC(G5)
Apr 21	56768.89	98.92	4800–9140	7.72	6.36	1500	1.90	LJT+YFOSC(G10)
May 16	56793.88	123.91	4080–9140	7.72	6.36	1500	1.34	LJT+YFOSC(G10)
Jul 24	56862.69	192.72	4300–9140	7.72	6.36	3530	1.32	LJT+YFOSC(G10)
Nov 11	56973.46	303.49	3000–9130	2.99	3.10	3600	1.15	NOT+ALFOSC(G4)

Note.
[a] The epoch is relative to the *V*-band maximum date, MJD = 56669.97.

Table A5
The Detailed Information of Compared Stars in Figures 4 and 5

Star	DM (mag)	$E(B-V)$ (mag)	t^R_{rise} (days)	$t^R_{1/2}$ (days)	$M^R_{\max}$ (mag)	$\Delta m_{15}(R)$ (mag)	Type	References
iPTF 13bvn	31.76	0.07	19.36	12.00	−17.00	1.09	Ib	(1, 2, 3, 4, 5,)
SN 2005bf[a]	34.50	0.05	42.47	18.68	−18.18	0.37	Ib/c	(6, 7, 8, 9)
SN 2007Y[a]	31.43	0.11	20.14	10.39	−16.43	0.81	Ib/IIb	(5, 10)
SN 2008D	32.46	0.60	19.60	13.18	−17.14	0.15	Ib	(5, 6, 11, 12)
SN 2009jf	32.65	0.16	21.44	14.08	−18.12	0.31	Ib	(6, 13, 14)
SN 2011fu	34.36	0.22	26.40	14.65	−18.35	0.51	IIb	(15)
SN 2005hg	34.87	0.09	16.97	12.18	−18.19	0.49	Ib/c	(6, 16, 17)
SN 2008ax	29.92	0.30	21.80	10.85	−17.57	0.74	IIb	(5, 18, 19)
SN 2019yvr[a]	30.84	0.56	17.64	11.27	−17.23	0.70	Ib	(20)
SN 2014C	30.89	0.70	12.13	7.28	−18.22	0.33	Ib	This work

Note.
[a] The samples use *r*-band magnitude in this table.
Reference. (1) M. C. Bersten et al. 2014; (2) Y. Cao et al. 2013; (3) C. Fremling et al. 2014; (4) G. Folatelli et al. 2016; (5) P. J. Brown et al. 2014; (6) F. B. Bianco et al. 2014; (7) G. Folatelli et al. 2006; (8) K. Maeda et al. 2007; (9) M. D. Stritzinger et al. 2018; (10) M. Stritzinger et al. 2009; (11) P. A. Mazzali et al. 2008; (12) M. Modjaz et al. 2009; (13) S. Valenti et al. 2011; (14) D. K. Sahu et al. 2011; (15) B. Kumar et al. 2013; (16) M. R. Drout et al. 2011; (17) M. Modjaz et al. 2014; (18) A. Pastorello et al. 2008; (19) D. Y. Tsvetkov et al. 2009; (20) L. Ferrari et al. 2024.

Table A6
Reference of the SNe in Figure 8

Star	(a) Pre-maximum	(b) Maximum	(c) 7 Days Post-maximum	(d) 14 Days Post-maximum
iPTF 13bvn	Y. Cao et al. (2013)	Y. Cao et al. (2013)	...	S. Srivastav et al. (2014)
SN 2004gq	M. Modjaz et al. (2014)	M. Modjaz et al. (2014)	...	M. Modjaz et al. (2014)
SN 2005bf	M. Modjaz et al. (2014)	G. Folatelli et al. (2006)	M. Modjaz et al. (2014)	...
SN 2007Y	M. Stritzinger et al. (2009)	...	M. Stritzinger et al. (2009)	I. Shivvers et al. (2019)
SN 2008D	I. Shivvers et al. (2019)	D. Malesani et al. (2009b)	I. Shivvers et al. (2019), M. Modjaz et al. (2009)	M. Modjaz et al. (2014)
SN 1997X	...	M. Modjaz et al. (2014)	M. Modjaz et al. (2014)	...
SN 1999ex	...	M. Hamuy et al. (2002)	Superfit[a]	M. Hamuy et al. (2002)
SN 2007C	...	I. Shivvers et al. (2019)	M. Modjaz et al. (2014)	I. Shivvers et al. (2019)

Note.
[a] http://www.dahowell.com/superfit.html

ORCID iDs

Jujia Zhang https://orcid.org/0000-0002-8296-2590
Paolo Mazzali https://orcid.org/0000-0001-6876-8284
Elena Pian https://orcid.org/0000-0001-8646-4858
Stefano Benetti https://orcid.org/0000-0002-3256-0016
Lina Tomasella https://orcid.org/0000-0002-3697-2616

References

Anderson, G. E., Horesh, A., Mooley, K. P., et al. 2017, MNRAS, 466, 3648
Arnett, W. D. 1982, ApJ, 253, 785
Arnett, W. D., Bahcall, J. N., Kirshner, R. P., & Woosley, S. E. 1989, ARA&A, 27, 629
Astropy Collaboration, Price-Whelan, A. M., Lim, P. L., et al. 2022, ApJ, 935, 167
Astropy Collaboration, Price-Whelan, A. M., Sipőcz, B. M., et al. 2018, AJ, 156, 123
Astropy Collaboration, Robitaille, T. P., Tollerud, E. J., et al. 2013, A&A, 558, A33
Barbon, R., Benetti, S., Cappellaro, E., Rosino, L., & Turatto, M. 1990, A&A, 237, 79
Bersten, M. C., Benvenuto, O. G., Folatelli, G., et al. 2014, AJ, 148, 68
Bhirombhakdi, K., Chornock, R., Miller, A. A., et al. 2019, MNRAS, 488, 3783
Bianco, F. B., Modjaz, M., Hicken, M., et al. 2014, ApJS, 213, 19
Bietenholz, M. F., Bartel, N., Kamble, A., et al. 2021, MNRAS, 502, 1694
Bietenholz, M. F., Kamble, A., Margutti, R., Milisavljevic, D., & Soderberg, A. 2018, MNRAS, 475, 1756
Blondin, S., & Tonry, J. L. 2007, ApJ, 666, 1024
Brethauer, D., Margutti, R., Milisavljevic, D., et al. 2022, ApJ, 939, 105
Brown, P. J., Breeveld, A. A., Holland, S., Kuin, P., & Pritchard, T. 2014, Ap&SS, 354, 89
Cao, Y., Kasliwal, M. M., Arcavi, I., et al. 2013, ApJL, 775, L7
Cappellaro, E., Mazzali, P. A., Benetti, S., et al. 1997, A&A, 328, 203
Chandra, P., Chevalier, R. A., Chugai, N., Milisavljevic, D., & Fransson, C. 2020, ApJ, 902, 55
Chatzopoulos, E., Wheeler, J. C., & Vinko, J. 2012, ApJ, 746, 121
Chatzopoulos, E., Wheeler, J. C., Vinko, J., Horvath, Z. L., & Nagy, A. 2013, ApJ, 773, 76
Chornock, R., Filippenko, A. V., Li, W., et al. 2011, ApJ, 739, 41
Chugai, N. N., & Chevalier, R. A. 2006, ApJ, 641, 1051
Dai, Z. G., Wang, S. Q., Wang, J. S., Wang, L. J., & Yu, Y. W. 2016, ApJ, 817, 132
Dessart, L., Hillier, D. J., Yoon, S.-C., Waldman, R., & Livne, E. 2017, A&A, 603, A51
Dessart, L., Yoon, S.-C., Aguilera-Dena, D. R., & Langer, N. 2020, A&A, 642, A106
Drout, M. R., Soderberg, A. M., Gal-Yam, A., et al. 2011, ApJ, 741, 97
Fan, Y.-F., Bai, J.-M., Zhang, J.-J., et al. 2015, RAA, 15, 918
Ferrari, L., Folatelli, G., Kuncarayakti, H., et al. 2024, MNRAS, 529, L33
Folatelli, G., Contreras, C., Phillips, M. M., et al. 2006, ApJ, 641, 1039
Folatelli, G., Van Dyk, S. D., Kuncarayakti, H., et al. 2016, ApJL, 825, L22
Foley, R. J., Berger, E., Fox, O., et al. 2011, ApJ, 732, 32
Foreman-Mackey, D., Hogg, D. W., Lang, D., & Goodman, J. 2013, PASP, 125, 306
Fransson, C., & Chevalier, R. A. 1987, ApJL, 322, L15
Fraser, M., Magee, M., Kotak, R., et al. 2013, ApJL, 779, L8
Fremling, C., Sollerman, J., Taddia, F., et al. 2014, A&A, 565, A114
Gal-Yam, A., Arcavi, I., Ofek, E. O., et al. 2014, Natur, 509, 471
Gehrels, N., Chincarini, G., Giommi, P., et al. 2004, ApJ, 611, 1005
Groh, J. H., Meynet, G., Ekström, S., & Georgy, C. 2014, A&A, 564, A30
Hamuy, M., Maza, J., Pinto, P. A., et al. 2002, AJ, 124, 417
Harkness, R. P., Wheeler, J. C., Margon, B., et al. 1987, ApJ, 317, 355
Harris, C. R., Millman, K. J., van der Walt, S. J., et al. 2020, Natur, 585, 357
Hunter, J. D. 2007, CSE, 9, 90
Immler, S., Modjaz, M., Landsman, W., et al. 2008, ApJL, 674, L85
Jacobson-Galán, W. V., Dessart, L., Davis, K. W., et al. 2024, ApJ, 970, 189
Kim, M., Zheng, W., Li, W., et al. 2014, CBET, 3777, 1
Kumar, B., Pandey, S. B., Sahu, D. K., et al. 2013, MNRAS, 431, 308
Lucy, L. B. 1991, ApJ, 383, 308
Maeda, K., Hattori, T., Milisavljevic, D., et al. 2015, ApJ, 807, 35
Maeda, K., Kawabata, K., Mazzali, P. A., et al. 2008, Sci, 319, 1220
Maeda, K., Mazzali, P. A., Deng, J., et al. 2003, ApJ, 593, 931
Maeda, K., Tanaka, M., Nomoto, K., et al. 2007, ApJ, 666, 1069
Malesani, D., Fynbo, J. P. U., Hjorth, J., et al. 2009a, ApJL, 692, L84
Malesani, D., Fynbo, J. P. U., Hjorth, J., et al. 2009b, in AIP Conf. Proc. 1111, Probing Stellar Populations Out to the Distant Universe: Cefalu 2008, Proceedings of the International Conference, ed. G. Giobbi et al. (Melville, NY: AIP), 627
Margutti, R., Kamble, A., Milisavljevic, D., et al. 2017, ApJ, 835, 140
Matheson, T., Filippenko, A. V., Li, W., Leonard, D. C., & Shields, J. C. 2001, AJ, 121, 1648
Mauerhan, J., Williams, G. G., Smith, N., et al. 2014, MNRAS, 442, 1166
Mauerhan, J. C., Filippenko, A. V., Zheng, W., et al. 2018, MNRAS, 478, 5050
Mauerhan, J. C., Smith, N., Filippenko, A. V., et al. 2013a, MNRAS, 430, 1801
Mauerhan, J. C., Smith, N., Silverman, J. M., et al. 2013b, MNRAS, 431, 2599
Mazzali, P. A., Deng, J., Maeda, K., et al. 2004, ApJ, 614, 858
Mazzali, P. A., Iwamoto, K., & Nomoto, K. 2000, ApJ, 545, 407
Mazzali, P. A., Kawabata, K. S., Maeda, K., et al. 2005, Sci, 308, 1284
Mazzali, P. A., & Lucy, L. B. 1998, MNRAS, 295, 428
Mazzali, P. A., Valenti, S., Della Valle, M., et al. 2008, Sci, 321, 1185
Milisavljevic, D., Fesen, R. A., Gerardy, C. L., Kirshner, R. P., & Challis, P. 2010, ApJ, 709, 1343
Milisavljevic, D., Margutti, R., Kamble, A., et al. 2015, ApJ, 815, 120
Modjaz, M., Blondin, S., Kirshner, R. P., et al. 2014, AJ, 147, 99
Modjaz, M., Li, W., Butler, N., et al. 2009, ApJ, 702, 226
Morales-Garoffolo, A., Elias-Rosa, N., Bersten, M., et al. 2015, MNRAS, 454, 95
Nomoto, K., Yamaoka, H., Pols, O. R., et al. 1994, Natur, 371, 227
Ofek, E. O., Sullivan, M., Shaviv, N. J., et al. 2014, ApJ, 789, 104
Orlando, S., Greco, E., Hirai, R., et al. 2024, ApJ, 977, 118
Pastorello, A., Cappellaro, E., Inserra, C., et al. 2013, ApJ, 767
Pastorello, A., Kasliwal, M. M., Crockett, R. M., et al. 2008, MNRAS, 389, 955
Pastorello, A., Smartt, S. J., Mattila, S., et al. 2007, Natur, 447, 829
Phillips, M. M., Simon, J. D., Morrell, N., et al. 2013, ApJ, 779, 38
Piro, A. L., & Nakar, E. 2013, ApJ, 769, 67
Poznanski, D., Ganeshalingam, M., Silverman, J. M., & Filippenko, A. V. 2011, MNRAS, 415, L81
Prieto, J. L., Brimacombe, J., Drake, A. J., & Howerton, S. 2013, ApJL, 763, L27
Roming, P. W. A., Kennedy, T. E., Mason, K. O., et al. 2005, SSRv, 120, 95
Sahu, D. K., Gurugubelli, U. K., Anupama, G. C., & Nomoto, K. 2011, MNRAS, 413, 2583
Schlafly, E. F., & Finkbeiner, D. P. 2011, ApJ, 737, 103
Science Software Branch at STScI, 2012 PyRAF: Python alternative for IRAF, Astrophysics Source Code Library, ascl:1207.011
Shivvers, I., Filippenko, A. V., Silverman, J. M., et al. 2019, MNRAS, 482, 1545
Smith, N. 2014, ARA&A, 52, 487
Soderberg, A. M., Berger, E., Page, K. L., et al. 2008, Natur, 453, 469
Sollerman, J., Fransson, C., Barbarino, C., et al. 2020, A&A, 643, A79
Srivastav, S., Anupama, G. C., & Sahu, D. K. 2014, MNRAS, 445, 1932
Stritzinger, M., Hamuy, M., Suntzeff, N. B., et al. 2002, AJ, 124, 2100
Stritzinger, M., & Leibundgut, B. 2005, A&A, 431, 423
Stritzinger, M., Mazzali, P., Phillips, M. M., et al. 2009, ApJ, 696, 713
Stritzinger, M. D., Anderson, J. P., Contreras, C., et al. 2018, A&A, 609, A134
Sun, N.-C., Maund, J. R., & Crowther, P. A. 2020, MNRAS, 497, 5118
Sun, N.-C., Maund, J. R., Crowther, P. A., et al. 2022, MNRAS, 510, 3701
Taddia, F., Stritzinger, M. D., Bersten, M., et al. 2018, A&A, 609, A136
Taubenberger, S., Navasardyan, H., Maurer, J. I., et al. 2011, MNRAS, 413, 2140
Taubenberger, S., Valenti, S., Benetti, S., et al. 2009, MNRAS, 397, 677
Thomas, B. P., Wheeler, J. C., Dwarkadas, V. V., et al. 2022, ApJ, 930, 57
Thomas, R. C., Nugent, P. E., & Meza, J. C. 2011, PASP, 123, 237
Tinyanont, S., Kasliwal, M. M., Fox, O. D., et al. 2016, ApJ, 833, 231
Tinyanont, S., Lau, R. M., Kasliwal, M. M., et al. 2019, ApJ, 887, 75
Tominaga, N., Tanaka, M., Nomoto, K., et al. 2005, ApJL, 633, L97
Tsvetkov, D. Y., Volkov, I. M., Baklanov, P., Blinnikov, S., & Tuchin, O. 2009, PZ, 29, 2
Turatto, M., Benetti, S., & Cappellaro, E. 2003, in From Twilight to Highlight: The Physics of Supernovae, ed. W. Hillebrandt & B. Leibundgut (Berlin: Springer), 200
Uomoto, A., & Kirshner, R. P. 1986, ApJ, 308, 685

Valenti, S., Benetti, S., Cappellaro, E., et al. 2008, MNRAS, 383, 1485
Valenti, S., Fraser, M., Benetti, S., et al. 2011, MNRAS, 416, 3138
Wang, C.-J., Bai, J.-M., Fan, Y.-F., et al. 2019, RAA, 19, 149
Yaron, O., Perley, D. A., Gal-Yam, A., et al. 2017, NatPh, 13, 510
Yoon, S. C., Woosley, S. E., & Langer, N. 2010, ApJ, 725, 940
Zhang, J., Dessart, L., Wang, X., et al. 2024, ApJL, 970, L18
Zhang, J., Lin, H., Wang, X., et al. 2023, SciBu, 68, 2548
Zheng, W., Li, W., Filippenko, A. V., & Cenko, S. B. 2014, ATel, 5721, 1